Rapidly Declining Hostless Type Ia Supernova KSP-OT-201509b from the KMTNet Supernova Program: Transitional Nature and Constraint on ^{56}Ni Distribution and Progenitor Type

Dae-Sik Moon[1], Yuan Qi Ni[1], Maria R. Drout[1,2], Santiago González-Gaitán[3,4], Niloufar Afsariardchi[1], Hong Soo Park[5], Youngdae Lee[5,6], Sang Chul Kim[5,7], John Antoniadis[8,9], Dong-Jin Kim[5], and Yongseok Lee[5,10]

[1] David A. Dunlap Department of Astronomy and Astrophysics, University of Toronto, 50 St. George Street, Toronto, ON M5S 3H4, Canada
moon@astro.utoronto.ca
[2] The Observatories of the Carnegie Institution for Science, 813 Santa Barbara Street, Pasadena, CA 91101, USA
[3] Centro de Modelamiento Matemático, Universidad de Chile, Beauchef 851, Piso 7, Santiago, Chile
[4] CENTRA, Instituto Superior Técnico—Universidade de Lisboa, Portugal
[5] Korea Astronomy and Space Science Institute, 776, Daedeokdae-ro, Yuseong-gu, Daejeon, 34055, Republic of Korea
[6] Department of Astronomy and Space Science, Chungnam National University, Daejeon 34134, Republic of Korea
[7] Korea University of Science and Technology (UST), Daejeon 34113, Republic of Korea
[8] Institute of Astrophysics, FORTH, Department of Physics, University of Crete, Voutes, University Campus, Heraklion, Greece
[9] Max-Planck-Institut für Radioastronomie, Bonn, Germany
[10] School of Space Research, Kyung Hee University, Yongin 17104, Republic of Korea
Received 2020 July 2; revised 2021 January 31; accepted 2021 February 2; published 2021 April 6

Abstract

We report the early discovery and multicolor (*BVI*) high-cadence light-curve analyses of the rapidly declining sub-Chandrasekhar Type Ia supernova KSP-OT-201509b (= AT 2015cx) from the KMTNet Supernova Program. The Phillips and color stretch parameters of KSP-OT-201509b are $\Delta M_{B,15} \simeq 1.62$ mag and $s_{BV} \simeq 0.54$, respectively, at an inferred redshift of 0.072. These, together with other measured parameters (such as the strength of the secondary *I*-band peak, colors, and luminosity), identify the source to be a rapidly declining Type Ia of a transitional nature that is closer to Branch-normal than 91bg-like. Its early light-curve evolution and bolometric luminosity are consistent with those of homologously expanding ejecta powered by radioactive decay and a Type Ia SN explosion with 0.32 ± 0.01 $M_\odot$ of synthesized ^{56}Ni mass, 0.84 ± 0.12 $M_\odot$ of ejecta mass, and $(0.61 \pm 0.14) \times 10^{51}$ erg of ejecta kinetic energy. While its $B - V$ and $V - I$ colors evolve largely synchronously with the changes in the *I*-band light curve, as found in other supernovae, we also find the presence of an early redward evolution in $V - I$ prior to -10 days since peak. The bolometric light curve of the source is compatible with a stratified ^{56}Ni distribution extended to shallow layers of the exploding progenitor. Comparisons between the observed light curves and those predicted from ejecta–companion interactions clearly disfavor Roche lobe–filling companion stars at large separation distances, thus supporting a double-degenerate scenario for its origin. The lack of any apparent host galaxy in our deep stack images reaching a sensitivity limit of $\sim$28 mag arcsec^{-2} makes KSP-OT-201509b a hostless Type Ia supernova and offers new insights into supernova host galaxy environments.

1. Introduction

It is well established that Type Ia supernovae (SNe Ia) originate from explosive thermonuclear runaways in a C–O white dwarf (WD; Hoyle & Fowler 1960), usually attributed to mass accretion from a nondegenerate binary companion or a merger/collision of two WDs. The former is known as the single-degenerate (e.g., Whelan & Iben 1973) scenario, the latter as the double-degenerate scenario (e.g., Iben & Tutukov 1984; Webbink 1984). Although the overall similarities in the observed light curves of SNe Ia are indicative of the presence of shared underlying core mechanisms, there exists substantial diversity in other observed properties, including uncertainties in the inferred accretion processes, explosion mechanisms, and nature of progenitors, as well as host galaxy environment. According to Li et al. (2001), for example, about one-third of nearby SNe Ia are peculiar. The cause of this diversity is not well understood and is under considerable debate (see Taubenberger 2017, for a recent review of peculiar SNe Ia).

Among these stands out the long-lasting question about the origin of the group of SNe Ia exhibiting rapid postpeak evolution identified with a large decline rate in light curves. This group of

SNe Ia is called "91bg-like," following its archetype SN 1991bg (Filippenko et al. 1992; Leibundgut et al. 1993), while the main population are "Branch-normal." When viewed on the Phillips relation (Phillips 1993; Phillips et al. 1999), which compares the peak luminosity and decline rate of SNe Ia using the parameter $\Delta M_{B,15}$ (= Phillips parameter) that measures the change in *B*-band magnitude during the first 15 days after peak, the 91bg-like rapid decliners appear as a distinctive group with $\Delta M_{B,15} \gtrsim 1.6$ mag (e.g., Taubenberger et al. 2008; Burns et al. 2014). It has been reported that a significant portion, i.e., 15%–20%, of the entire SN Ia population belongs to the group of rapid decliners (e.g., Li et al. 2011b; Srivastav et al. 2017) accompanied by a low peak luminosity in most cases (e.g., Howell 2001; Taubenberger et al. 2008). While normal SNe Ia typically show double-peaked light curves in the *I* and near-infrared bands, where the primary first peak precedes that of the *B* band, the rapid decliners show a single *I*-band peak after they reach the maximum brightness in the *B* band (see Taubenberger et al. 2008; Dhawan et al. 2017, and references therein). This behavior is known to be related to ^{56}Ni production and the evolution of temperature and opacity in

SNe Ia, with the 91bg-like group being driven by a smaller amount of ^{56}Ni. These faint and rapidly declining SNe Ia have mostly been found in large elliptical galaxies and are therefore thought to be associated with old stellar populations (Howell 2001; Sullivan et al. 2006; González-Gaitán et al. 2011).

The distinction of this group of rapid decliners from the normal SNe Ia in the Phillips relation, however, is less apparent when the decline rate is represented by the color stretch parameter ($= s_{BV}$), defined as the time span between the B-band maximum and that of the $B - V$ color normalized by 30 days (Burns et al. 2014). The rapid decliners tend to transition to the postpeak decline phase dominated by ^{56}Co decay in less than 15 days, which leads to a discontinuity in the slope of the Phillips relation near $\Delta M_{B,15} \simeq 1.6$ mag and makes it inapplicable for $\Delta M_{B,15} \gtrsim 1.6$ mag. The disappearance of the clear distinction between Branch-normal and 91bg-like based on the s_{BV} parameterization of the decline rate suggests that the SNe Ia in the two groups may in fact be similar kinds with a continuous distribution of observables that appear to be separated by a gap in the number of observed samples between them.

There is no clear consensus yet on whether or not the rapidly declining SNe Ia, or at least some of them, indeed have different origins from the rest. Some favor different origins for the rapid decliners, usually relying on the double-degenerate sub-Chandrasekhar (sub-Ch) mass explosions or the deflagrations in rotating WDs (see Taubenberger et al. 2008; Dhawan et al. 2017, and references therein), while others have argued that Chandrasekhar-mass explosions can explain at least some of them, often associated with delayed detonations (e.g., Mazzali et al. 2007; Ahsall et al. 2018). Based on the results of extensive radiative transport simulations, Goldstein & Kasen (2018) reported that SNe Ia with a large $\Delta M_{B,15}$, i.e., $\gtrsim 1.55$ mag, can only be produced by sub-Ch-mass explosions. This is more or less consistent with the slightly broader criterion $\Delta M_{B,15} \gtrsim 1.4$ mag obtained by using non-local thermodynamic equilibrium calculations of light curves (Blondin et al. 2017). In contrast, Hoeflich et al. (2017) reported that a uniform explosion based on Chandrasekhar-mass spherical delayed detonations can explain most of the observed light curves of SNe Ia without the need for a separate mechanism for (extreme) rapid decliners.

A key clue to understanding the origin of the division between the two groups of Branch-normal and 91bg-like SNe Ia lies in the nature of the so-called transitional SNe Ia straddling them. The identification of a statistically significant number of such transitional SNe with a continuous distribution of observed properties could support the common-origin hypothesis. The light curves of the transitional SNe Ia are usually featured with a large Phillips parameter and a B-band peak between two I-band peaks. Their prototypical case is SN 1986G (Phillips et al. 1987), observed with $\Delta M_{B,15} \simeq 1.81$ mag, which is substantially larger than the $\Delta M_{B,15} \sim 1.1$ mag of Branch-normal, and a low explosion energy (Phillips et al. 1987; Ashall et al. 2016), showing a very rapid decay in postpeak evolution. Spectroscopically, however, it appears to be very similar to normal SNe Ia, thereby revealing its intermediate nature. The Phillips parameter of the transitional types lies roughly within the range of $\Delta M_{B,15} \simeq 1.5$–1.8 mag (Prieto et al. 2006; Ashall et al. 2016; Srivastav et al. 2017; Gall et al. 2018). However, transitional types have also been identified in SNe Ia beyond this range, while some SNe Ia within the range have been observed with no clear signs of intermediate properties (e.g., Taubenberger et al. 2008; Hsiao et al. 2015). According to

Taubenberger et al. (2008), SNe Ia with $\Delta M_{B,15}$ in the range of 1.75–1.85 mag show an inconspicuous secondary I-band peak and can be considered as the intermediate group between Branch-normal and 91bg-like, whereas those in the range of $\Delta M_{B,15} =$ 1.5–1.75 mag featured with a double-peaked I-band light curve, relatively small luminosity, and rapid decay are similar to normal types. Hsiao et al. (2015) suggested that rapidly declining SNe Ia are of a transitional nature if they show two long-wave-band (i.e., $iYJHK$) peaks in the light curves with the first and primary peak preceding the B-band peak. The 10 transitional SNe Ia compiled in their work show $\Delta M_{B,15} \simeq 1.30$–1.80 mag and $s_{BV} \simeq 0.46$–0.86 with average values of 1.62 mag ($\Delta M_{B,15}$) and 0.70 (s_{BV}). These transitional SNe Ia have been observed mostly in non-star-forming galaxies (Mazzali et al. 2007; Ashall et al. 2016), similar to 91bg-like events (see above).

In this paper, we present multicolor, high-cadence observations of the SN Ia KSP-OT-201509b (or AT 2015cx), which appears to be a rapidly declining SN Ia of transitional nature that is more similar to Branch-normal than 91bg-like, providing a rare opportunity to investigate the early photometric evolution of rapid decliners. In addition, the absence of any apparent host galaxy for this SN in our deep stack images reaching $\mu_{BVI} \sim 28$ mag arcsec^{-2} implies that such SNe Ia can occur in host galaxy environments that are quite different from what have been previously reported. In Section 2, we provide the details of our discovery and monitoring observations of KSP-OT-201509b, followed by the analyses of the observed light curves and color evolution, as well as template fitting in Section 3. We compare the observations and model predictions in Sections 4 and 5: comparisons of the bolometric light curve with model predictions based on different types of ^{56}Ni distribution (Section 4) and the observed early light curves with model light curves expected from the interactions between ejecta and companion in SNe Ia (Section 5). We show that there is no apparent host galaxy of KSP-OT-201509b in Section 6 and provide the summary and conclusion in Section 7.

2. Observations

We conducted high-cadence, multicolor (BVI) monitoring observations of a $2° \times 2°$ field containing the galaxy NGC 300 in the direction of the south Galactic pole using the Korea Microlensing Telescope Network (KMTNet; Kim et al. 2016) as part of its KMTNet Supernova Program (KSP; Moon et al. 2016; Afsariardchi et al. 2019). The initial phase of the monitoring started in 2015 July during the commissioning test period of the KMTNet and continued until 2017 August 9. The KMTNet operates three wide-field 1.6 m telescopes located at the Cerro Tololo Inter-American Observatory (CTIO; Chile), the South African Astronomical Observatory (SAAO), and the Siding Spring Observatory (SSO; Australia). All three of the telescopes are equipped with a CCD camera with a $2° \times 2°$ field of view (FoV) at $0.''4$ pixel sampling with Johnson–Cousins $BVRI$ filters (Kim et al. 2016). We obtained about 2460 images of the field with 60 s exposure time for each of the BVI bands, and the mean cadence of our observations within the monitoring period was approximately 3.5 hr for each band. The typical limiting magnitude for a point source detected with a signal-to-noise ratio (S/N) greater than 2 in the individual images was ~ 22 mag when the seeing was better than $2''$.

A new point source was detected in our B-band image obtained with the SAAO telescope at 21.56 hr on 2015 September 24 (UT), or MJD 57,289.89825, with a magnitude of 21.29 ± 0.37 mag at
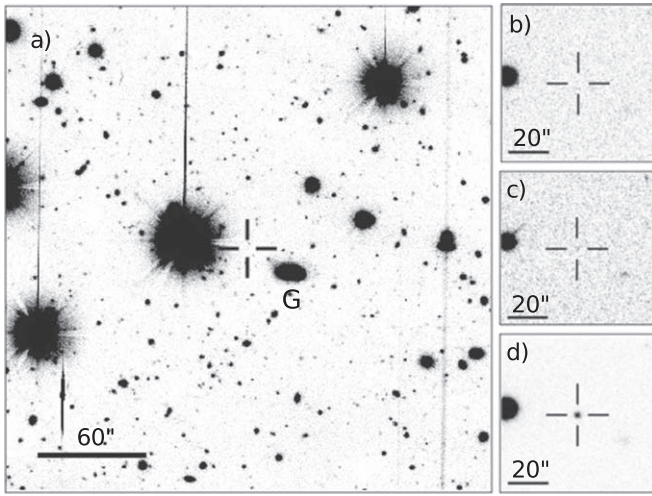
Figure 1. (a) Deep KMTNet *I*-band image centered on the location of KSP-OT-201509b obtained by stacking individual exposures taken when the source was below the detection limit. North is up, and east is to the left. The crosshair marks the location of KSP-OT-201509b, whereas the letter G denotes the apparently extended source ~27″ away in the southwestern direction from the SN (see Sections 2 and 6). Panels (b)–(d) are individual 60 s *B*-band images focused on the location of KSP-OT-201509b: (b) the image obtained 7.2 hr prior to the first detection of the source, (c) the first detection image obtained at MJD = 57,289.89825, and (d) the image with the peak observed brightness obtained 14.1 days from the first detection.

Table 1
Observed Magnitudes of KSP-OT-201509b

Time (MJD)	Magnitude[a] (mag)	Error (mag)	Band
57,289.89826	21.292	0.368	*B*
57,289.90000	21.447	0.333	*V*
57,289.91440	21.648	0.487	*B*
57,289.91770	21.587	0.322	*I*
57,289.93130	20.971	0.283	*B*
57,289.93338	21.332	0.277	*V*
57,289.96603	21.036	0.297	*B*
57,289.96760	21.195	0.208	*V*
57,289.98403	21.517	0.355	*V*
57,289.98574	21.267	0.246	*I*
57,289.99826	21.188	0.320	*B*
57,290.00235	21.652	0.308	*I*

Notes. Sample of the observed magnitudes of KSP-OT-201509b during its early phase. All of the observed magnitudes of KSP-OT-201509b are available online.

[a] The *B*- and *V*-band magnitudes are in the Vega system, while the *I*-band magnitudes are in the AB system (see text).

(This table is available in its entirety in machine-readable form.)

the coordinates (R.A., decl.) = (00^{h}57^{m}03^{s}19, −37°02′23″6) (J2000). The source was subsequently detected in the *V* band 2 minutes later with 21.45 ± 0.33 mag and in the *I* band 28 minutes later with 21.59 ± 0.32 mag, while it was not detected in a *B*-band image obtained 7.18 hr before the first detection. We name this source KSP-OT-201509b. It remained above the detection limit over the ensuing period of 4 months at the same location, reaching observed peak magnitudes of 18.59 ± 0.02 (*B*), 18.49 ± 0.02 (*V*), and 18.91 ± 0.05 (*I*) mag over ~18 days. Figure 1 presents images of the field centered on the location of KSP-OT-201509b. In the figure, panel (a) is a deep *I*-band image that reaches a sensitivity limit $\mu_I \simeq 27.8$ mag arcsec^{-2} created by stacking 1167 individual images obtained either before the first detection of the source or after its disappearance. The image stacking is made using the SWARP package (Bertin et al. 2002). Each individual frame is subtracted by its own background estimated with a background mesh size of 512 pixels and then resampled and median combined with other frames to create the final stack image. Only the individual frames whose seeing is better than 2″ are used, which can help mitigate the effects of the confusion limit in image stacking (e.g., Ashcraft et al. 2018). There exists no underlying source at the location of KSP-OT-201509b in the stack image. The three other panels, (b)–(d), are the individual 60 s *B*-band images for the last nondetection exposure obtained 7.18 hr prior to the first detection (b), the first detection (c), and the image from MJD 57,304.04163, when the source reached peak brightness (d).

The photometric calibration is carried out using more than 10 nearby standard reference stars within 15′ distance from KSP-OT-201509b available in the AAVSO Photometric All-Sky Survey[11] database. Only the reference stars whose apparent magnitudes are in the range of 15–16 mag are used to secure

high S/Ns in their flux measurement while avoiding CCD saturation and nonlinearity effects. A local point-spread function (PSF), which is obtained by fitting a Moffat function (Moffat 1969; Trujillo et al. 2001) and sky background emission to the reference stars, is fitted for the measurements of fluxes of KSP-OT-201509b and the reference stars. The AAVSO photometric system consists of the standard Johnson *BV* and the Sloan *i* band, i.e., *BVi*. The calibration of the KMTNet *B*-band data against the Johnson *B*-band magnitudes of the AAVSO system requires a color correction given by $\Delta B \simeq 0.27\,(B - V) + $ offset (Park et al. 2017, 2019), where ΔB is the *B*-band magnitude differences between the magnitudes obtained in KMTNet images before color correction and the standard magnitudes of AAVSO reference stars in the database. The same *B*-band color dependence in our data is identified, and the *B*-band magnitudes of the AAVSO reference stars used in our photometric calibration are corrected with their known $B - V$ colors. The final *B*-band magnitudes of KSP-OT-201509b are obtained after applying *S*-correction for SNe by following the procedure described in Stritzinger et al. (2002) using template spectra from the SNooPy package (see Section 3.3). No such color dependence has been identified in the KMTNet *V* and *I* bands when calibrated against the AAVSO *V* and *i* bands, respectively (Park et al. 2017, 2019), which is also confirmed in the data for KSP-OT-201509b. Thus, the photometric calibration of our KMTNet *VI*-band data is made against the AAVSO *Vi* bands without any color correction. As a result, the *BV*-band magnitudes of KSP-OT-201509b presented in this paper are in the Vega magnitude system, while its *I*-band magnitudes are in the AB system. Table 1 contains a sample of the observed magnitudes of KSP-OT-201509b.

According to the dust map of Schlegel et al. (1998), the total Galactic reddening in the direction of KSP-OT-201509b is $E(B - V) \simeq 0.013$ mag. Using the updated $R_V = 3.1$ dust model of Schlafly & Finkbeiner (2011), we find a corresponding extinction of 0.046, 0.034, and 0.021 mag in the *B*, *V*, and *i* bands, respectively. The small extinction is compatible with the location of KSP-OT-201509b near the Galactic pole. Since no host galaxy is identified for the source (see below and Section 6), only this

---

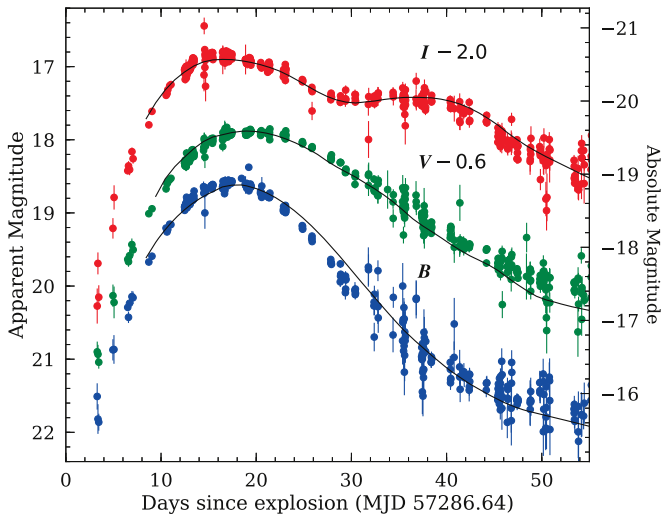[11] The AAVSO Photometric All-Sky Survey Data Release 9, https://www.aavso.org/apass.

Figure 2. The *BVI* light curves of KSP-OT-201509b observed with the KMTNet: blue, green, and red circles for the *B*, *V*, and *I* bands, respectively. The abscissa represents days from the estimated explosion epoch (MJD 57,286.64) of the source, which is adopted to be equal to the epoch of first light (see Section 3.1 and Table 2) in the observer frame; the ordinate does the observed apparent magnitudes (left) and corresponding absolute magnitudes (right) at the DM of 37.47 mag (see Section 3.3). The *V*- and *I*-band magnitudes are shifted vertically by -0.6 and -2.0 mag, respectively, to separate the overlapping light curves of the three bands. For the several initial epochs at the beginning, adjacent individual exposures are binned together to increase the S/Ns. The black solid lines represent the best-fit template to all of the *BVI*-band light curves obtained from SNooPy fitting after *S*-correction with $z = 0.072$ (see Section 3.3).

(The data used to create this figure are available.)

small Galactic extinction is taken into account in our extinction correction.

One notable feature in Figure 1(a) is the absence of any underlying host galaxy candidate for KSP-OT-201509b at its location or in the immediate vicinity of the source in our deep *I*-band image. The absence is also confirmed in the *B* and *V* bands. The most conspicuously extended nearby object of KSP-OT-201509b is located at (R.A., decl.) $\simeq$ ($00^{h}57^{m}01\overset{s}{.}23$, $-37°02'37\overset{''}{.}5$) (J2000), $\sim 27''$ away in the southwest. Hereafter, we call this object G, as we denote in the figure. In order to measure the redshift and understand the nature of G, we conducted spectroscopic observations of the source using the Low Dispersion Survey Spectrograph 3[12] on the 6.5 m Magellan Clay telescope on 2016 August 11. We used the VHP-All grism coupled with a $1''$ slit for dispersion and obtained a single 600 s exposure. See Section 6 for the spectrum of G and its analysis.

3. Light Curves and Classification of KSP-OT-201509b as a Rapidly Declining Transitional SN Ia

3.1. Light Curves and Epoch of First Light

Figure 2 shows the *BVI*-band light curves of KSP-OT-201509b obtained with the KMTNet for about 2 months. Over approximately the first 2 weeks, the source gradually ascends to its peak brightness, more than 3 mag brighter than that of the first detection. The observed peak brightnesses are 18.59, 18.49, and 18.91 mag for the *B*, *V*, and *I* bands, respectively. (See Table 2 for

Table 2
Parameters of KSP-OT-201509b

Parameter	Value
(R.A., decl.) (J2000)	($00^{h}57^{m}03\overset{s}{.}19$, $-37°02'23\overset{''}{.}64$)
First detection: UT and MJD	$21^{h}33^{m}29^{s}$ on 2015 September 24 and 57,289.89825
Peak epoch (t_{p})[a]: UT and MJD	$1^{h}55^{m}$ on 2015 October 10 and 57,305.08
Observed peak magnitudes	18.59 (*B*), 18.49 (*V*), 18.91 (*I*) mag
Observed peak epochs[b]	-1.11 (*B*), 1.29 (*V*), -2.77 (*I*) days
Redshift (z)	0.072 ± 0.003
Phillips parameter ($\Delta M_{B,15}$)	1.62 ± 0.03 mag
Color stretch parameter (s_{BV})	0.54 ± 0.05
Absolute peak magnitude	-18.94 (*B*), -18.93 (*V*), -18.38 (*I*) mag
Early light power-law index (α)	2.0 ± 0.2 (*B*), 1.9 ± 0.2 (*V*), 2.1 ± 0.2 (*I*)
Epoch of first light (t_{0})[b]	-18.4 ± 0.6 days
First detection from epoch of first light	3.3 ± 0.6 days
Peak bolometric luminosity and epoch	$(9.0 \pm 0.3) \times 10^{42}$ erg s^{-1} and -0.5 ± 0.6 days
^{56}Ni mass (M_{Ni})	$0.32 \pm 0.01~M_{\odot}$
Ejecta mass (M_{ej})	$0.84 \pm 0.12~M_{\odot}$
Ejecta kinetic energy (E_{K})	$(0.61 \pm 0.14) \times 10^{51}$ erg

Notes. All date and time values are given in the observer frame.
[a] The epoch of the peak *B*-band brightness determined in the SNooPy template fitting.
[b] This is relative to t_{p}.

the observed and estimated parameters of KSP-OT-201509b.) There exist clear band-dependent differences in the manner of how postpeak decay evolves in Figure 2. The *B*-band decay is much faster than that of the other bands, while the *I*-band light curve is featured with a secondary peak about 2 weeks after the first and primary peak, which precedes the *B*-band peak. We estimate the average strength of the secondary *I*-band peak within 20–40 days after the epoch of the *B*-band peak to be $\langle I \rangle_{20-40} = 0.309 \pm 0.002$ with respect to the maximum brightness of the first and primary peak of the *I* band (Krisciunas et al. 2001). The overall evolution of the observed light curves of KSP-OT-201509b—which includes the initial ascent in brightness, the presence of a secondary peak in the *I* band, the absence of any apparent postpeak plateau or linear phase, and the slow decay—identifies KSP-OT-201509b as an SN Ia powered by radioactive decay of ^{56}Ni and ^{56}Co (e.g., Hamuy et al. 1996). We compare in Figure 3 the *I*-band light curve (black) of KSP-OT-201509b with those of four well-sampled SNe Ia: SN 2011fe (red), SN 1994D (blue), SN 2005ke (cyan), and SN 2005bl (green). The first two are Branch-normal with $\Delta M_{B,15} \simeq 1.1$ and 1.4 mag, respectively, whereas the last two are 91bg-like with more rapid postpeak decline rates, $\Delta M_{B,15} \simeq 1.7$ (SN 2005ke) and 1.9 (SN 2005bl) mag. The postpeak decline rate of KSP-OT-201509b in Figure 3 appears to be intermediate between the two groups.

Figure 4 presents the observed early light curves of KSP-OT-201509b prior to 8 days before the peak, normalized by its peak brightness. Power laws have been adopted to describe the evolution of the early light curves of SNe Ia when intensities are substantially lower (e.g., <40%; see Olling et al. 2015) than the peak intensity, since the brightness of an ^{56}Ni-powered expanding homologous sphere mediated by the photon diffusion process is expected to be $\propto t^2$, where *t* is time (e.g., Nugent et al. 2011). We fit the early light curves of KSP-OT-201509b during the first ~ 10 days of its detection in Figure 4 with a power law $F(t) \propto (t - t_0)^{\alpha}$,
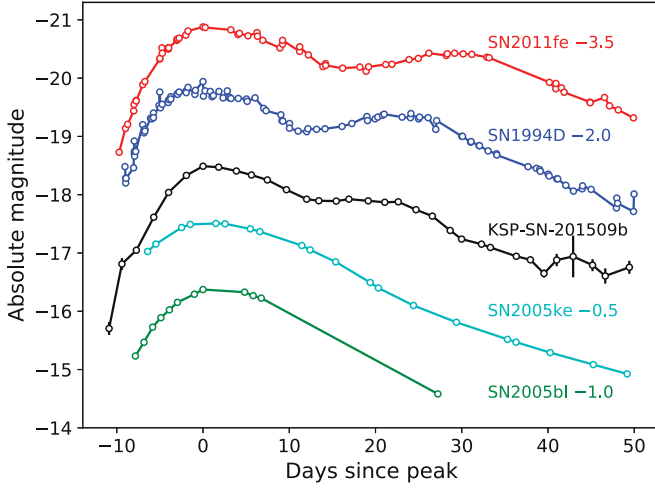
Figure 3. Comparison of the *I*-band light curve of KSP-OT-201509b (black) with those of four other well-sampled SNe Ia in increasing order of postpeak decline rate from top to bottom. The light curves are aligned with the epochs of their respective *I*-band peak in the source rest frame. The top two light curves are for SN 2011fe (red; shifted by −3.5 mag) and SN 1994D (blue; shifted by −2.0 mag; Wu et al. 1995; Pereira et al. 2013, and references therein). They have $\Delta M_{B,15} \simeq 1.1$ and 1.4 mag, respectively. The bottom two light curves are for SN 2005ke (cyan; shifted by −0.5 mag) and SN 2005bl (green; shifted by −1.0 mag), which have $\Delta M_{B,15} \simeq 1.7$ and 1.9 mag, respectively (Contreras et al. 2010).
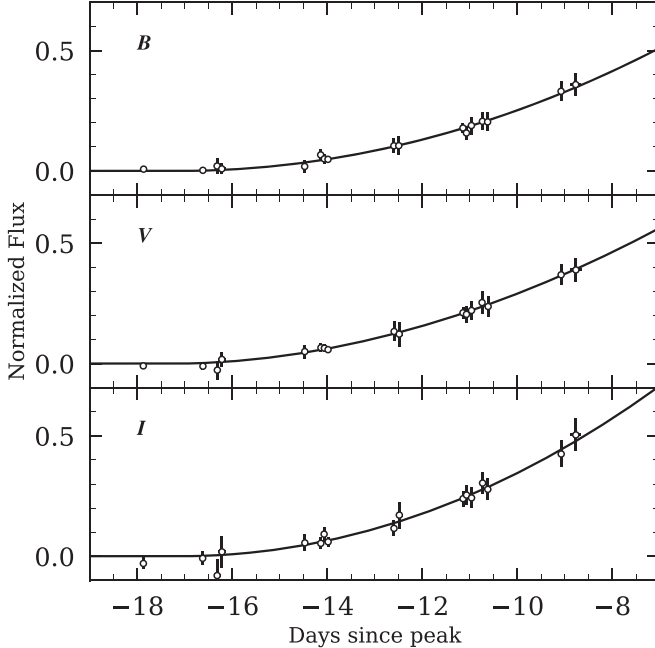
Figure 4. Early *BVI* (top to bottom) light curves (open circles) of KSP-OT-201509b normalized by the peak intensity of each band. Three to seven adjacent individual flux measurements, each obtained with 60 s exposure time, are binned together to increase the S/Ns, and the error bars correspond to the 95% confidence level of the flux measurement. The solid lines are the best-fit power laws obtained for each band. The abscissa represents days from the epoch of the peak *B*-band brightness estimated by SNooPy fitting in the source rest frame.

where F and t_0 represent the observed brightness and epoch of first light, respectively. The best-fit power-law indices are $\alpha = 2.0 \pm 0.2$ (*B*), 1.9 ± 0.2 (*V*), and 2.1 ± 0.2 (*I*), and the epoch of first light is $t_0 = -18.4 \pm 0.6$ days since the peak in the observer frame, or -17.2 ± 0.5 days in the rest frame. (See Section 3.3 for
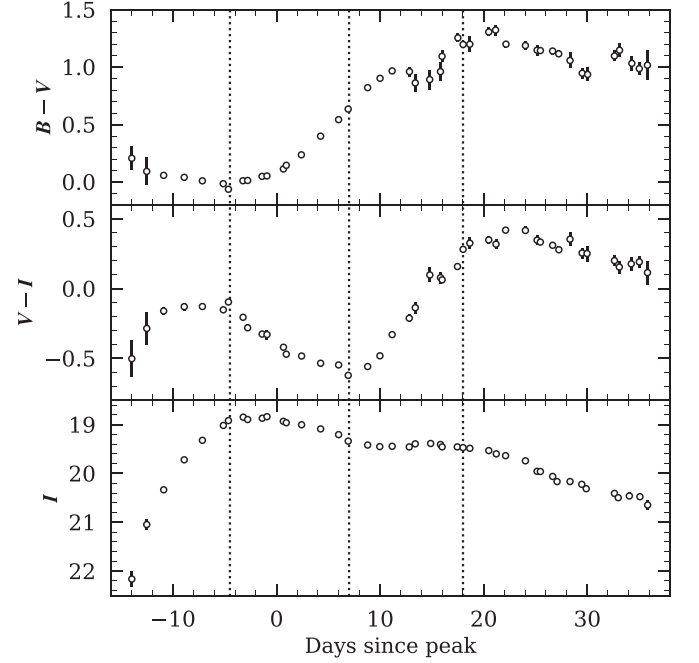

Figure 5. Evolution of the $B - V$ (top panel) and $V - I$ (middle panel) colors of KSP-OT-201509b aligned with the *I*-band light curve (bottom panel). The data are binned up to a 1 day interval to increase the S/Ns, and the error bars represent the uncertainties measured at the 68% confidence level. The abscissa represents days from the epoch of the peak *B*-band brightness estimated in SNooPy fitting in the source rest frame. The three vertical dotted lines mark three notable color epochs of −4.5, 7, and 18 days.

the estimation of the epoch of peak brightness and the redshift of the source.) The fitted power-law indices are $\simeq 2$, as expected for a homologous expansion, similar to what has been found in other SNe Ia (e.g., Nugent et al. 2011; Olling et al. 2015; Dimitriadis et al. 2019). We also estimate the epoch of first light using a Gaussian process extrapolation that can provide a less model-dependent inspection of the epoch. The Gaussian process extrapolation-based epoch of first light is -16.4 ± 0.5 days (rest frame) for the *BVI* light curves, which is slightly smaller than but consistent with -17.2 ± 0.5 days from our power-law fitting. We adopt -17.2 ± 0.5 days as the epoch of explosion of KSP-OT-201509b in its rest frame.

3.2. Color Evolution

Figure 5 shows the evolution of the $B - V$ and $V - I$ colors of KSP-OT-201509b aligned with that of the *I*-band light curve. The three vertical dotted lines mark three color epochs over which the colors show a notable phase transition in their evolution. The first and third color epochs are −4.5 and +18 days, respectively, from the epoch of the *B*-band peak brightness estimated using SN template fitting of the observed *BVI*-band light curves (see below for details). These two color epochs roughly correspond to those of the primary and secondary *I*-band peaks, respectively. The second color epoch is +7 days, which is close to the midpoint between the first and third epochs, near the onset of the *I*-band secondary rise.

We summarize the evolution of the $B - V$ and $V - I$ colors, which are largely synchronous with that of the *I* band, as follows.

1. Prior to the first color epoch of −4.5 days, the $B - V$ color starts at $\simeq 0.2$ mag around −14 days, or ∼3.3 days in the

rest frame since the epoch of first light (Table 2), and slowly becomes bluer to $\simeq 0.0$ mag in about 10 days near the first color epoch. The blueward evolution of the $B - V$ during this early phase of KSP-OT-201509b appears to be consistent with that of the early red population of SNe Ia, which comprises predominantly Branch-normal types (Stritzinger et al. 2018). It is thought to be due mainly to the heating from ^{56}Ni radioactive decay as the deeper layer of the ejecta is revealed (see Hoeflich et al. 2017). Indeed, we show in Section 4 that the observed early light curves of KSP-OT-201509b can be explained by a shallow ^{56}Ni distribution (e.g., Piro & Morozava 2016) leading to an early increase in color temperature. The $V - I$ color of KSP-OT-201509b during this phase, on the other hand, shows a redward evolution from approximately -0.5 to -0.1 mag within the first 2 days before it stalls relatively flat until the first color epoch. The SNe in general have rarely been observed with $V - I$ colors at these early epochs, and the origin of the early redward evolution of KSP-OT-201509b is unclear. It is conceivable, however, that the evolution of spectral features—e.g., Ca II features in the I band (Parrent et al. 2012, see Figure 1 therein)—are responsible for it.

2. Across the first color epoch of -4.5 days, when the I-band light curve nears its primary peak, both colors change the direction of their evolution, in that $B - V$ becomes redder while $V - I$ becomes bluer. We attribute this redward evolution in $B - V$ to the absorption by iron-peak elements (e.g., Hoeflich et al. 2017), whereas the blueward evolution in $V - I$ is attributed to a temperature increase.

3. The $B - V$ color evolves redward relatively monotonically between the first (i.e., -4.5 days) and third (i.e., $+18$ days) color epochs, which is largely equivalent to the period between the two I-band peaks, by $\simeq 1.2$ mag, whereas the $V - I$ color changes its direction of evolution again around the second color epoch (i.e., $+7$ days) from blueward to redward until it reaches the third color epoch. This is due to the recombination process of Fe III leading to a rebrightening in the I band by redistribution of blue/UV radiation (e.g., Kasen 2006; see also Section 1). We note that the Fe III recombination also plays a critical role in determining the color evolution of SNe Ia in the near-infrared wave bands with respect to their light curves (Dhawan et al. 2015), similar to what we report here.

4. After the third color epoch, both colors gradually evolve blueward as the SN enters the Lira law phase known to have a linear blueward evolution for an extended period (Phillips et al. 1999).

5. The $B - V$ and $V - I$ colors at the peak epoch in Figure 5 are 0.056 and -0.34 mag, respectively. According to Taubenberger et al. (2008), the observed $B - V$ color of KSP-OT-201509b at the peak epoch is significantly bluer than the 0.4–0.7 mag range known for 91bg-like, while it is consistent with the value expected for an SN Ia with $\Delta M_{B,15} \lesssim 1.75$ mag.

6. The SNe Ia with $\Delta M_{B,15}$ in the range of 1.5–1.75 mag are known to show an initial blueward evolution between -10 and 10 days in $V - I$ followed by a rapid redward evolution (Taubenberger et al. 2008), as observed in KSP-OT-201509b, while this initial blueward evolution is absent in 91bg-like. It is quite noteworthy, however,

that the $V - I$ color evolution of KSP-OT-201509b in Figure 5 also reveals that the initial blueward evolution (between -10 and 10 days) is in fact preceded by an earlier redward evolution at <-10 days, as explained above. A similar $V - I$ color pattern at comparably early epochs has been observed in SN 1994D, which is a normal but relatively overluminous SN Ia (Patat et al. 1996).

7. Overall, the observed color evolutions of KSP-OT-201509b are compatible with what can be expected from an SN Ia with $\Delta M_{B,15} = 1.62$ mag as measured for the source (see Section 3.3) and appear to be more similar to Branch-normal than 91bg-like. Also, the similarity of its color evolutions to those observed in other SNe Ia indicates that there is an insignificant extinction by its potential host galaxy, as we assumed (Section 2).

3.3. Template Fitting and Parameters of KSP-OT-201509b

In order to estimate the key physical parameters of KSP-OT-201509b as an SN Ia, we conduct template fitting of its observed light curves (Figure 2) using two SN Ia light-curve templates from the SN template fitting package SNooPy (v181212; Burns et al. 2011), one for Branch-normal and the other for 91bg-like. Because no spectroscopic observations were made for KSP-OT-201509b (due to its detection during the commissioning test period of the KMTNet) and its host galaxy is unknown (see Section 6), we estimate its distance using an iterative template model fitting technique. For this, we adopt a set of 100 trial redshifts in the range $z = 0.03$–0.1 for the potential redshifts of the source. This corresponds to the distance modulus (DM) of $\simeq 35.6$–38.6 mag based on the cosmological model of Riess et al. (2016) with parameters $H_0 \simeq 73.24$ km s^{-1} Mpc^{-1}, $\Omega_M \simeq 0.27$, and $\Omega_\Lambda \simeq 0.73$. Note that these cosmological parameters are more recently updated values that are slightly different from those adopted in the SNooPy package internally, which are $H_0 \simeq 72$ km s^{-1} Mpc^{-1}, $\Omega_M \simeq 0.28$, and $\Omega_\Lambda \simeq 0.73$ (Spergel et al. 2007). Given the $B = 18.59 \pm 0.02$ peak apparent magnitude of KSP-OT-201509b (Table 2), this redshift range ensures that we investigate the full range of peak absolute magnitudes typically displayed by SNe Ia, which is between -17 and -20 mag, as shown in Figure 6, for the conceivable peculiar motion of the source (see below). We use SNooPy to conduct SN template fitting and K-corrections with the input redshifts, assuming no host galaxy extinction.

Figures 7 and 8 show the results of our template fitting to the light curves of KSP-OT-201509b. In Figure 7, we compare the observed V- (top panel) and I-band (bottom panel) light curves of the source with the best-fit template light curves for Branch-normal (solid line) and 91bg-like (dashed line). We exclude the B-band light curve in this initial template fitting stage to avoid the uncertainties involved in the S-correction process (see Section 2). While the best-fit V-band light curve from the Branch-normal template in the figure appears to give a good match to the observed light curve, that from the 91bg-like template slightly overpredicts the decline rate immediately after the peak. This discrepancy is more obvious in the I band, where the double-peaked light curve of KSP-OT-201509b is apparently incompatible with the best-fit 91bg-like template, showing that the source is more similar to Branch-normal than 91bg-like.
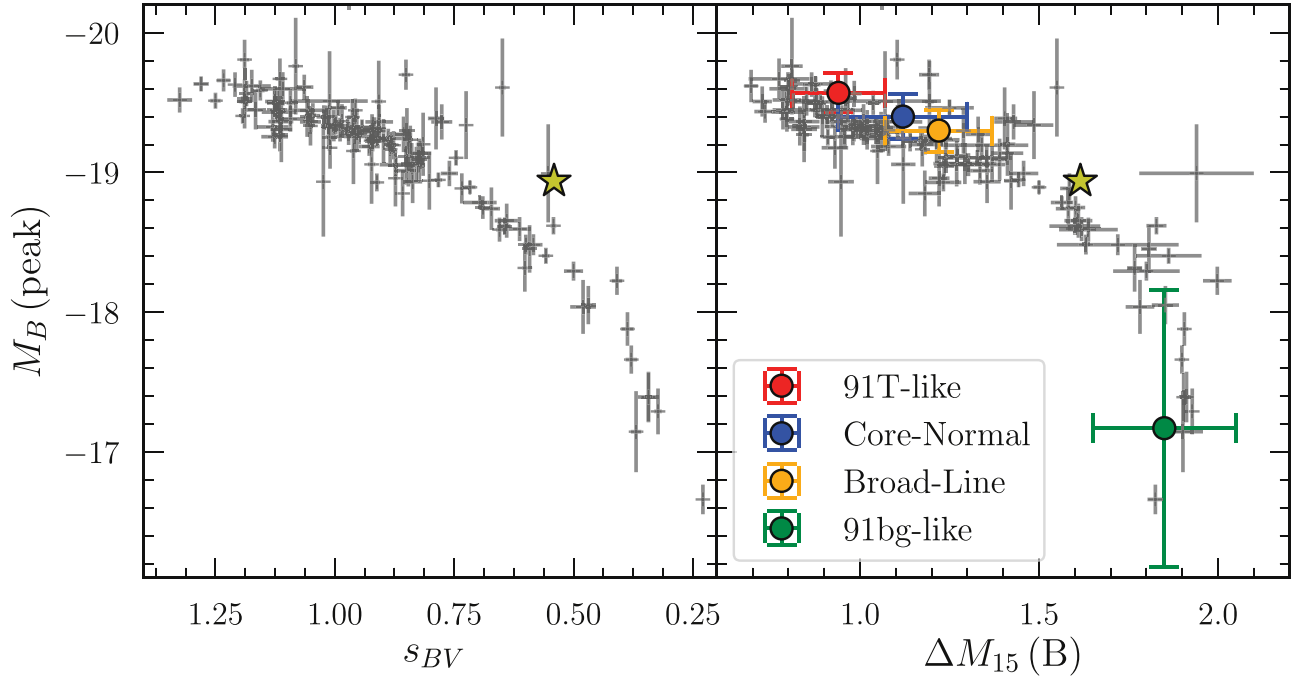
Figure 6. (Left panel) Distribution of s_{BV} and the B-band peak absolute magnitude (plus signs) of SNe Ia compiled in Burns et al. (2018) with those of KSP-OT-201509b (yellow star). (Right panel) Same as the left panel but for $\Delta M_{B,15}$. Also shown are the mean values of the four major subtypes of SNe Ia from Parent et al. (2014): 91T-like (filled red circle), core-normal (filled blue circle), broad-line (filled orange circle), and 91bg-like (filled green circle).
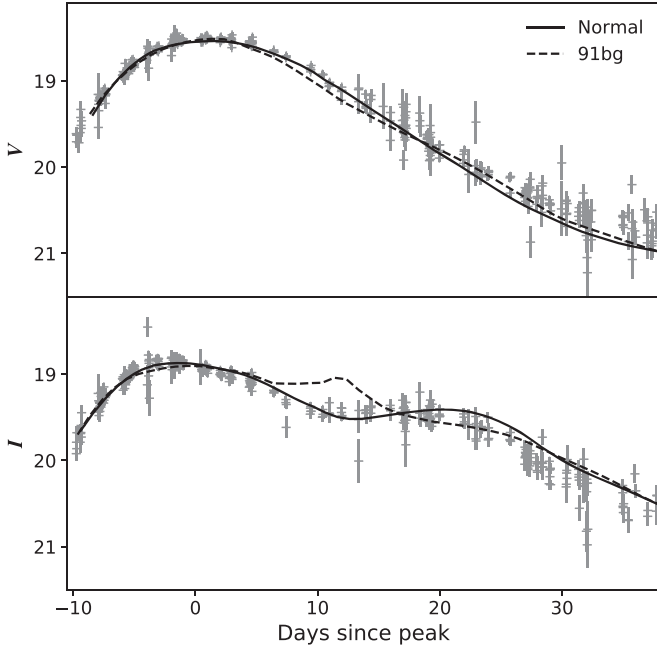

Figure 7. (Top panel) Observed V-band light curve of KSP-OT-201509b overlaid on that of the best-fit SN Ia Branch-normal (solid line; $z = 0.072$) and 91bg-like (dashed line; $z = 0.077$) templates obtained from SNooPy fitting. The abscissa represents days from the epoch of the peak B-band brightness estimated in SNooPy fitting in the observer frame. (Bottom panel) Same as the top panel but for the I-band light curve of KSP-OT-201509b.

Figure 8. Distribution of template fitting parameters of the KSP-OT-201509b light curves in SNooPy as a function of 100 trial redshifts in the range $z = 0.03$–0.10. The abscissae represent the trial redshift (bottom) and the corresponding cosmological DM (top), DM(z), consistent with the cosmological model of Riess et al. (2016). The shaded region highlights the inferred redshift range $z = 0.072 \pm 0.003$ of the source. (Top panel) Distribution of the offset, Δ(DM) (left axis), between the best-fit DM in SNooPy and the cosmological DM for a given redshift and the required peculiar velocity, v_{pec} (right axis), reconciling the DM offset as shown. The solid line is for Branch-normal template fitting; the dashed line is for the 91bg-like template. (Bottom panel) Same as the top panel but for the best-fit s_{BV} (left axis) at a given redshift and $\Delta M_{B,15}$ (right axis) calculated with s_{BV} using the relation between the two parameters in Burns et al. (2014).

Figure 8 presents the distribution of the fitted parameters from the template fitting as a function of the trial redshifts (bottom abscissa) or corresponding cosmological DM (top abscissa). The top panel shows Δ(DM) (left ordinate), which is the offset between the SNooPy-fitted DM at a given redshift and the cosmological DM from the top abscissa, representing
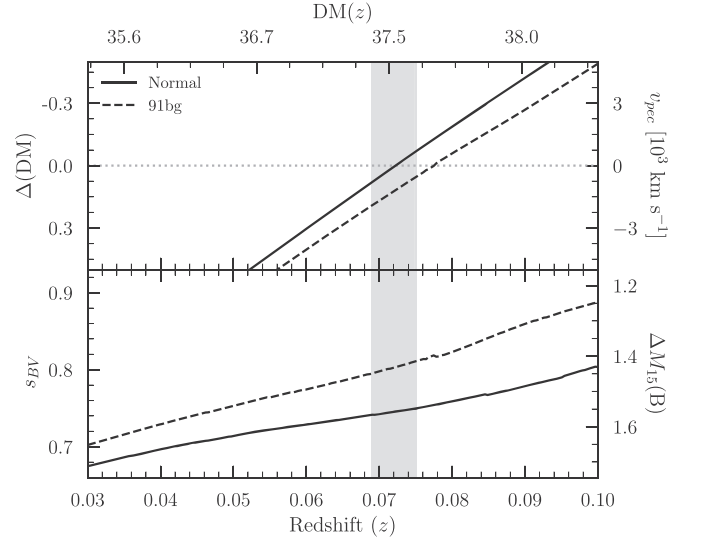
the peculiar motion (as calculated in the right ordinate) of KSP-OT-201509b if the fitted DM and assumed redshift are indeed the real values for the source. As in the figure, no peculiar motion of KSP-OT-201509b is required if the source is located at $z = 0.072$ for Branch-normal (solid line) or 0.077 for 91bg-

like (dashed line). At redshifts smaller than 0.06 or larger than 0.08, in order for the input redshift and the cosmological redshift from the DM obtained in the SNooPy fitting to be comparable, the required peculiar motions become significantly larger, i.e., $>1000 \text{ km s}^{-1}$, than what can be expected from KSP-OT-201509b (see below) for the Branch-normal template fitting. This also applies to the 91bg-like template fitting but at slightly larger redshift values.

In the bottom panel of Figure 8, the distribution of the best-fit color stretch parameter s_{BV} (left ordinate) increases along the trial redshifts as the quality of the fitting becomes poorer. The growing incompatibility between the template and observed light curves at a higher redshift, caused mainly by the secondary I-band peak, results in larger best-fit values of the color stretch parameter for higher trial redshifts. The Phillips parameters ($\Delta M_{B,15}$; right ordinate) in the panel are obtained using the relation between s_{BV} and $\Delta M_{B,15}$ in Burns et al. (2014). At $z = 0.072$, the best-fit s_{BV} is 0.75 (or $\Delta M_{B,15} = 1.54 \text{ mag}$) for Branch-normal, while it is 0.82 (or $\Delta M_{B,15} = 1.39 \text{ mag}$) for 91bg-like at $z = 0.077$. The χ^2_R values of the best-fit templates at these redshifts are $\simeq 2$ for Branch-normal ($z = 0.072$) and $\simeq 3$ for 91bg-like ($z = 0.077$). Overall, the best-fit Branch-normal templates give systematically, although slightly, smaller χ^2_R values of $\lesssim 3$ for all trial redshifts. At higher redshifts $z \gtrsim 0.08$, however, χ^2_R values of the best-fit 91bg-like templates become increasingly greater than 3.

Based on the results shown in Figures 7 and 8 from the SNooPy template fitting, we estimate the redshift of KSP-OT-201509b to be $z = 0.072 \pm 0.003$ and conclude that the source is closer to Branch-normal than 91bg-like as follows. First of all, the comparison between the observed and best-fit templates (Figure 7), especially the I-band comparison (bottom panel), gives a clear preference for Branch-normal for KSP-OT-201509b. Also, the best-fit color stretch parameter $s_{BV} \simeq 0.82$ for the 91bg-like template is unacceptably larger than those found in 91bg-like SNe, while the best-fit $s_{BV} \simeq 0.75$ for Branch-normal is largely acceptable, although somewhat small, for a Branch-normal SN. This shows that the 91bg-like template is apparently incompatible with the observed light curves of KSP-OT-201509b at an admissible redshift range. The estimated redshift of KSP-OT-201509b is largely derived from the conceivable range of reasonable proper motions for its progenitor. As explained in Section 6, it is highly likely that the host of KSP-OT-201509b is an unidentified dwarf galaxy whose brightness is fainter than ~ 25 mag in BVI. In the local environment around the Milky Way, the peculiar velocities of dwarf galaxies are at a level of 200 km s^{-1} (Lewis et al. 2007), with a few occasional outliers showing higher velocities in special environments (e.g., Drinkwater et al. 2001). For a galaxy like the Milky Way, ~ 500 km s^{-1} is the escape velocity, while rare objects with faster velocities of up to ~ 1000 km s^{-1} are considered hypervelocity stars (Brown 2015; Boubert et al. 2017). Adopting 500 km s^{-1} as a conservative, or upper-limit, assessment of the potential peculiar motion of KSP-OT-201509b, we obtain $\Delta z = 0.003$ as the uncertainty of the best-fit redshift from the Branch-normal template fitting after taking the uncertainty in the DM measurement from the SNooPy fitting, which includes the uncertainty contributions from the SNooPy template calibration and from adopting the more recently updated cosmological parameters than SNooPy (see above), and the uncertainty corresponding to 500 km s^{-1} peculiar motion into account together. The $\sim 4\%$ level of the photometric redshift uncertainty is comparable with what have been found in some other photometric studies of SNe Ia (e.g.,

Palanque-Delabrouille et al. 2010). This gives $z = 0.072 \pm 0.003$ and DM $= 37.47 \pm 0.10$ mag, or a luminosity distance of 311.9 Mpc, for the source (Figure 8). The small difference between the best-fit redshifts of Branch-normal and 91bg-like indicates that any potential systematic uncertainties resulting from applying the Branch-normal template to KSP-OT-201509b, which shows a transitional nature (Section 3.4), for its redshift determination is small.

We now conduct S-correction of the B-band light curve using this redshift and the spectral time series of the best-fit Branch-normal template shown in Figure 7, as identified in the VI-band light-curve analyses above. (Note that the B-band light curve in Figure 2 is the one obtained after S-correction.) We then use SNooPy with all of the S-corrected BVI light curves to obtain the best-fit Branch-normal template for KSP-OT-201509b (Figure 2, black lines) from which we derive K-corrections. We adopt the epoch of the B-band peak brightness, $t_p = 57{,}305.08 \pm 0.03$ (MJD), of the best-fit template, which is 15.18 ± 0.03 days after the epoch of first detection and ~ 18.4 days after the epoch of first light, as the peak epoch of KSP-OT-201509b from the template. Using the S- and K-corrected BVI curves of the SN in the rest frame, we estimate absolute peak magnitudes of -18.94 ± 0.01 (B), -18.93 ± 0.01 (V), and -18.38 ± 0.01 (I) mag with their respective epochs. We finally estimate the color stretch and Phillips parameters of KSP-OT-201509b to be $s_{BV} = 0.54 \pm 0.05$ using the B-band light curve and $B - V$ color evolution of the source as defined in Burns et al. (2014) and $\Delta M_{B,15} = 1.62 \pm 0.03$ mag by conducting polynomial fitting of the B-band light curve in the rest frame of $z = 0.072$. These final s_{BV} and $\Delta M_{B,15}$ values are different from those obtained from the VI-band template fitting above (i.e., $s_{BV} \simeq 0.75$ and $\Delta M_{B,15} \simeq 1.54$ mag for Branch-normal; $s_{BV} \simeq 0.82$ and $\Delta M_{B,15} \simeq 1.39$ mag for 91bg-like), and we attribute the discrepancy to the transitional nature of KSP-OT-201509b (see below), since neither template is an intrinsically good match to the observed light curves of the source. See Table 2 for the compilation of the physical parameters of KSP-OT-201509b.

As described above, the redshift of KSP-OT-201509b is estimated using its observed peak brightness by allowing the reasonable peculiar motion of the source in the frame of the SNooPy template fitting, rather than purely based on the goodness of the light-curve fitting. The minimum χ^2_R values of the SNooPy template fittings change only slightly, i.e., mostly between 2 and 3, over the trial redshift range of 0.01–0.1, making the parameter inadequate to discern the redshift of the source alone. In order to examine the validity of our redshift estimation from the SNooPy-based analyses, we apply two other SN Ia light-curve fitting packages to the observed light curves of KSP-OT-201509b. We first use the SALT2 fitting package (Guy et al. 2007) with the same trial redshift range of 0.01–0.1, which results in only a slight variation, i.e., between 4 and 5, of the minimum χ^2_R values, as we find in the SNooPy fitting. Both the best-fit redshifts from the SALT2 fitting of the B- and V-band light curves determined by the minimum χ^2_R value are consistently ~ 0.07, similar to what we obtain for KSP-OT-201509b from the SNooPy-based analyses above, while it is ~ 0.02 for the I band. This significant discrepancy between the BV and I bands might be due to incompatibility between the SALT2 package and the transitional nature of KSP-OT-201509b, which is expected to affect the I-band fitting more than the other bands, although it is important to note that
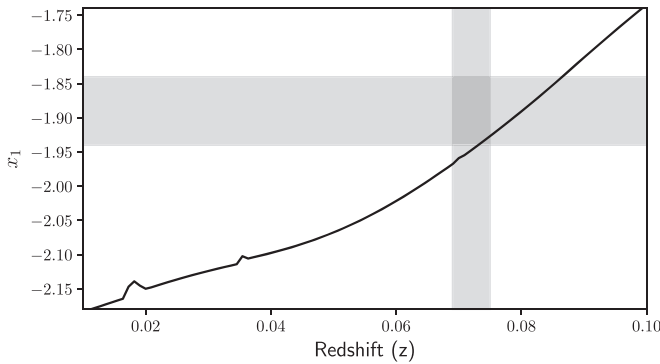
Figure 9. The solid line shows the distribution of the best-fit stretch parameter x_1 from the SALT2 fitting of the *VI*-band light curves of KSP-OT-201509b along the input redshift range of 0.01–0.1. The vertical shaded area represents $z = 0.072 \pm 0.003$, which is the redshift of the source based on our SNooPy analysis. The horizontal shaded area represents $x_1 = -1.89 \pm 0.05$, which is from the known conversion between s_{BV} and x_1 (Burns et al. 2014) for $s_{BV} = 0.745 \pm 0.005$ that we obtain in Figure 8 (bottom panel) from the SNooPy *VI*-band light-curve fitting.

these best-fit redshifts are poorly constrained given the small variations in the minimum χ^2_R values. Figure 9, which shows the distribution of the best-fit shape parameter ($= x_1$) from our SALT2 fitting of the KSP-OT-201509b light curves over the trial redshift range of 0.01–0.1, provides a consistency check between the SNooPy- and SALT2-based fitting results. In the figure, the two shaded areas represent the ranges of the redshift and x_1 expected from the SNooPy fitting for KSP-OT-201509b; the vertical shaded area is $z = 0.072 \pm 0.003$, which we estimate as the redshift of the source, while the horizontal shaded area is $x_1 = -1.89 \pm 0.05$, converted from the fitted s_{BV} values in Figure 8 (bottom panel) for the redshift using the known relationship between x_1 and s_{BV} in Burns et al. (2014). The SALT2-based x_1 parameter intersects the two shaded areas, showing that the results of the SNooPy fitting are consistent with those of the SALT2 fitting on the known relation between s_{BV} and x_1. In addition to the SALT2 fitting, we also apply the SiFTO SN fitting package (Conley et al. 2008) to the observed light curves of KSP-OT-201509b over the trial redshift range of 0.01–0.1. Although the best-fit redshift from the SiFTO fitting is poorly constrained again due to the small variation in the minimum χ^2_R values, we obtain ~0.07 for the best-fit redshift, compatible with SNooPy and SALT2 fitting results.

3.4. Transitional Nature of KSP-OT-201509b

The observed characteristics and measured parameters of KSP-OT-201509b identify the source as a rapidly declining SN Ia of a transitional nature that is more similar to Branch-normal than 91bg-like as follows. The rapidly declining nature of the source is easily confirmed in Figure 6 (left panel), where we compare the *B*-band peak absolute magnitude and s_{BV} of KSP-OT-201509b (yellow star) with those of the group of SNe Ia (plus signs) from Burns et al. (2018). The number of SNe gradually decreases as the s_{BV} values decrease (or the peak *B*-band luminosities become smaller) in the figure. After the location of KSP-OT-201509b at $s_{BV} \simeq 0.54$, the gradual distribution of the SNe identified with larger s_{BV} values disappears, and there exists only a small number of SNe as s_{BV} decreases in this range. The right panel of Figure 6, where $\Delta M_{B,15}$ is used instead of s_{BV} for the postpeak decline rate for the same SNe Ia as in the left panel, shows the mean $\Delta M_{B,15}$ values of the four major subtypes of SN Ia

(see Parrent et al. 2014): 91T-like (filled red circle), core-normal (filled blue circle), broad-line (filled orange circle), and 91bg-like (filled green circle), as well as that ($\Delta M_{B,15} \simeq 1.62$ mag) of KSP-OT-201509b (yellow star). Note that the SNe Ia in the 91T-like group are slowly evolving and overluminous, whereas core-normal and broad-line constitute Branch-normal. Bridging the gap between Branch-normal and 91bg-like in the figure, KSP-OT-201509b clearly appears to be associated with a small number of SNe Ia, showing its transitional nature.

In Burns et al. (2014), SNe Ia with $s_{BV} \lesssim 0.5$ show an *I*-band peak ~3–4 days later than *B*-band peak, while those with $s_{BV} \gtrsim 0.7$ are ~2–3 days earlier. The *I*-band peak of KSP-OT-201509b precedes that of the *B* band by about 1.5 days, which, together with its $s_{BV} \simeq 0.54$, places the source in the gap connecting the two populations. The relative strength of the secondary *I*-band peak is $\langle I \rangle_{20\text{–}40} = 0.309 \pm 0.002$ for KSP-OT-201509b (Section 3.1). The estimated values of s_{BV} and $\langle I \rangle_{20\text{–}40}$ of KSP-OT-201509b follow the overall correlation between the two parameters compiled for SNe Ia in the paper. The value $\simeq 0.309$ is low for Branch-normal but high for 91bg-like (Krisciunas et al. 2001; Burns et al. 2014; Srivastav et al. 2017), consistent with the interpretation that KSP-OT-201509b is of a transitional nature. Comparison of the source with other SNe Ia in terms of s_{BV}, $\langle I \rangle_{20\text{–}40}$, and the time delay between the *B*- and *I*-band peaks shows that it overlaps with "cool" (CL) objects (Burns et al. 2014, see Figure 6 therein), which are mostly rapid decliners but close to the boundary with the group of slow decliners, supporting the rapidly evolving and transitional nature of KSP-OT-201509b.

The $B - V$ color of KSP-OT-201509b at the peak epoch is $\simeq 0.08$ mag, and this is consistent with what has been found in transitional SNe Ia (Gall et al. 2018). While the source is transitional, the measured values of $\Delta M_{B,15}$ and s_{BV}, the presence of the secondary *I*-band peak, the overall color evolution, and the results of the template fitting all show that it is more similar to Branch-normal than 91bg-like. According to Dhawan et al. (2017), fast-declining SNe Ia more luminous than 5×10^{42} erg s^{-1} make a smooth connection to normal SNe Ia as we find in KSP-OT-201509b, whose peak bolometric luminosity is $(9.0 \pm 0.3) \times 10^{42}$ erg s^{-1} (Table 2, and see Section 4).

4. Bolometric Light Curve and ^{56}Ni Distribution

The radioactive decay of ^{56}Ni followed by that of ^{56}Co drives the light curves of SNe Ia after explosion. We compare here the bolometric light curve of KSP-OT-201509b with those expected from two different types of model ^{56}Ni distribution—centrally concentrated and stratified—in order to investigate how ^{56}Ni was distributed in the progenitor of the source, as well as its explosion parameters of ejecta mass and kinetic energy. During the photospheric phase of an SN Ia, when the expansion is driven by homologous spherical shocks within the first ~30 days after the explosion, the majority of its emission falls within the ultraviolet–optical–infrared (UVOIR) wave band (Contardo et al. 2000). We integrate the best-fit SN Ia template of KSP-OT-201509b that we obtained from the SNooPy template fitting (Section 3.3) over the rest-frame UVOIR wave band, or $\lambda = 3075\text{–}23763$ Å, to construct its bolometric light curve.[13] Figure 10 shows the bolometric light curve of KSP-OT-201509b (filled

---

[13] We note that a bolometric light curve obtained in this way is sometimes called a quasi-bolometric light curve (e.g., Blondin et al. 2017), given the limited wavelength range over which the luminosity is calculated. Since the difference is expected to be very small, we will call it a bolometric luminosity light curve throughout this paper for simplicity.

black circles), wherein the peak bolometric luminosity and epoch are $(9.0 \pm 0.3) \times 10^{42}$ erg s^{-1} and -0.5 ± 0.6 days, respectively.

4.1. Centrally Concentrated ^{56}Ni Distribution

In the case where the distribution of ^{56}Ni is strongly peaked toward the center of the ejected mass and the ejecta opacity is constant during SN explosion, the radioactively powered luminosity of an SN Ia during the photospheric phase can be described as (Arnett 1982, 1996; Valenti et al. 2008)

$$L(x) = M_{\mathrm{Ni}} \, e^{-x^2} \times [(\epsilon_{\mathrm{Ni}} - \epsilon_{\mathrm{Co}}) \, C(x) + \epsilon_{\mathrm{Co}} \, D(x)], \quad (1)$$

where M_{Ni} is the total mass of ^{56}Ni. The parameter x represents a scaled time dimension of SN explosion as

$$x = \frac{t}{\tau_m} \, , \quad \tau_m = \left(\frac{\kappa}{\beta_{\mathrm{A}} c}\right)^{1/2} \left(\frac{6 M_{\mathrm{ej}}^3}{5 E_{\mathrm{ej}}}\right)^{1/4} , \quad (2)$$

where t is the time since explosion, τ_m is the geometric mean of the diffusion and expansion timescales, κ is the opacity, $\beta_{\mathrm{A}} = 13.8$ is a model constant for SN density distribution, c is the speed of light, and M_{ej} and E_{ej} are the mass and kinetic energy of the ejecta, respectively. We adopt $\kappa = 0.1$ cm^2 g^{-1} dominated by the line transitions of ^{56}Ni during the photospheric phase (Pinto & Eastman 2000; Piro & Nakar 2014). In Equation (1), $\epsilon_{\mathrm{Ni}} = 3.90 \times 10^{10}$ and $\epsilon_{\mathrm{Co}} = 6.78 \times 10^{9}$ erg s^{-1} g^{-1} are the energy production rates per gram of ^{56}Ni and ^{56}Co, respectively. The term $C(x)$ is related to the luminosity produced by the nuclear reaction decay of ^{56}Ni, and so is $D(x)$ but to ^{56}Co. The equation shows that the luminosity of an SN Ia in this model is mainly determined by two parameters: the mass of ^{56}Ni (M_{Ni}) and the mean timescale (τ_m).

If we simply assume that the onset of the model is the same as that of the first light obtained from the power-law fit (Section 3.1), which gives 16.7 days as the time interval between the epochs of first light and peak bolometric luminosity (or "rise time"), we obtain $M_{\mathrm{Ni}} = 0.44 \pm 0.01 \, M_{\odot}$ and $\tau_m = 14.07 \pm 0.67$ days for the source by applying Equation (1) at the bolometric peak. This is equivalent to fixing Equation (1) using only two parameters, the peak bolometric luminosity and the rise time, regardless of the shape of the light curve. Figure 10 compares the model light curve (blue dotted line) predicted by the two obtained parameters, i.e., M_{Ni} and τ_m, with the bolometric light curve (black circles) of KSP-OT-201509b, where we can clearly identify overprediction of the bolometric luminosity by the model across the peak, showing that this method is inappropriate. This incompatibility is also confirmed with the inferred ejecta mass and kinetic energy of the source, which are $M_{\mathrm{ej}} = 1.86 \pm 0.24 \, M_{\odot}$ and $E_{\mathrm{ej}} = 1.35 \pm 0.30 \times 10^{51}$ erg, respectively, obtained under the assumption of a typical ejecta velocity $v_{\mathrm{ej}} = (11{,}000 \pm 1000)$ km s^{-1} (Scalzo et al. 2019) and $E_{\mathrm{ej}} = \frac{3}{10} M_{\mathrm{ej}} v_{\mathrm{ej}}^2$ for an SN Ia. The inferred ejecta mass and kinetic energy are unacceptably large for a fast-evolving SN Ia (Scalzo et al. 2019). This discrepancy is mainly due to the long rise time (16.7 days) and the fast postpeak decline rate ($\Delta M_{B,15} \simeq 1.62$ mag) of the source that are largely incompatible with the model of Equation (1). In other words, while this model may accurately estimate the total ^{56}Ni mass based on the peak luminosity of KSP-OT-201509b (see below), it is likely insufficient to reproduce the detailed evolution of the ascending and/or declining phases.
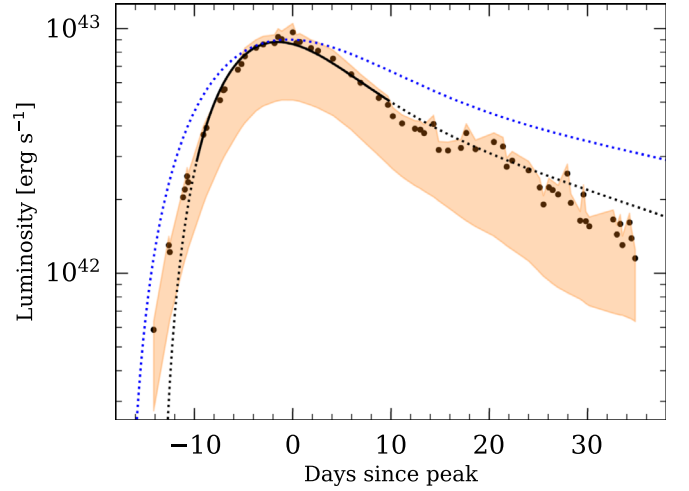

Figure 10. Bolometric light curve (filled black circles) of KSP-OT-201509b obtained by integrating the best-fit template over the wavelength range of 3075–23763 Å. The pumpkin shaded region represents the area between the upper and lower limits of the estimated bolometric luminosities. The upper limits are calculated by taking the uncertainties in photometric measurements and redshift into account, whereas the lower limits are bolometric luminosities integrated over the isophotal wavelength range of the *BVI* bands only. The abscissa is days from the epoch of the peak *B*-band brightness determined by SNooPy fitting in the source rest frame. The blue dotted line is for the bolometric luminosities calculated by Equation (1) for the centrally concentrated ^{56}Ni distribution when the onset of the model and the epoch of peak brightness are fixed to be the epoch of first light ($= t_0$) estimated in the power-law fitting of early light curves (Section 3.1) and that of the peak bolometric luminosity, respectively. The black solid line represents the predictions by Equation (1) obtained when only the bolometric light curve within ± 10 days around the peak is used in model fitting. The black dotted line is the extrapolation of the black solid line to earlier and later epochs beyond the interval of the ± 10 days around the peak by the same fitted parameters.

In order to obtain more reliable SN explosion parameters that match the evolution of the luminosity around the peak of KSP-OT-201509b, we conduct the fitting of Equation (1) to the bolometric light curve of KSP-OT-201509b (Figure 10) but limiting the period between -10 and $+10$ days across the peak in the fitting. This method, which excludes the early and late parts of the light curve, should provide more reliable explosion parameters, since it is less affected by the assumed ^{56}Ni distribution in Equation (1) and more dependent on the bulk properties of the ejecta. The best-fit parameters obtained this way are $M_{\mathrm{Ni}} = 0.32 \pm 0.01 \, M_{\odot}$ and $\tau_m = 9.45 \pm 0.52$ days, which provide a significantly improved match to the observed bolometric light curve around the peak with $\chi_{\mathrm{R}}^2 \simeq 0.42$ (Figure 10, black solid line). The inferred ejecta mass and kinetic energy are $M_{\mathrm{ej}} = 0.84 \pm 0.12 \, M_{\odot}$ and $E_{\mathrm{ej}} = (0.61 \pm 0.14) \times 10^{51}$ erg, respectively, consistent with what has been observed in other fast-evolving SNe (Dhawan et al. 2018; Scalzo et al. 2019; Wygoda et al. 2019). We therefore adopt these values as the explosion parameters of KSP-OT-201509b. In this model fit, we also note that -13.5 ± 0.4 days in the SN rest frame is the onset of the model light curves powered by centrally concentrated ^{56}Ni distribution, which is approximately 3.7 days after the epoch of first light (t_0; see Section 3.1). The difference of 3.7 days implies again that the centrally concentrated ^{56}Ni distribution in Equation (1) is inadequate to properly model the observed early light curves of KSP-OT-201509b, although it is capable of providing reliable SN explosion parameters when fitting is limited to the light curves around the peak. In Figure 10, the black dotted line shows the extrapolated model prediction of Equation (1) for early (< -10 days) and late (> 10 days) epochs using the explosion

parameters obtained in the fitting above. The best-fit model apparently underpredicts the bolometric luminosities at early epochs. We attribute this underprediction and the aforementioned difference between t_0 and the onset of the model light curves to a shallow ^{56}Ni distribution in KSP-OT-201509b, as we detail in Section 4.2.

The ejecta mass $M_{\rm ej} = 0.84 \pm 0.12$ $M_\odot$ places KSP-OT-201509b in the group of sub-Ch-mass SNe Ia, consistent with the results from previous studies of SNe Ia that rapid decliners are from sub-Ch-mass explosions (e.g., Scalzo et al. 2019). Note that, by assuming a smaller opacity, $\kappa = 0.08$ cm^2 g^{-1} (e.g., Arnett 1982; Li et al. 2019), we obtain ejecta mass and kinetic energy $M_{\rm ej} = 1.05 \pm 0.15$ $M_\odot$ and $E_{\rm ej} = (0.76 \pm 0.18) \times 10^{51}$ erg, respectively, still within the limit of the sub-Ch-mass explosion. Recent results from extensive radiation transport simulations also indicate that rapid decliners are highly unlikely to be from Chandrasekhar or super-Chandrasekhar-mass explosions (Goldstein & Kasen 2018).

4.2. Stratified ^{56}Ni Distribution

As shown above, the presence of early excess emission to what is expected by Equation (1) (Figure 10) and the difference of 3.7 days between the epoch of first light t_0 and the onset of the model light curves of Equation (1) indicate that the real ^{56}Ni distribution of KSP-OT-201509b is different from the simple central concentration assumed in Arnett (1982). It is conceivable, as recently suggested (Piro & Nakar 2014; Piro & Morozava 2016; Contreras et al. 2018; Magee et al. 2020; Magee & Maguire 2020), that there exists ^{56}Ni distributed close to the progenitor surface responsible for the early excess and the difference of 3.7 days. We investigate this possibility below based on these models.

4.2.1. Analytic Model

According to Piro & Nakar (2014, hereafter PN14), a stratified ^{56}Ni distribution extended more toward the surface can adequately model the bolometric light curves of other SNe Ia, such as SN 2009ig, SN 2011fe, and SN 2012cg. They modeled the local mass fraction of ^{56}Ni in the ejecta following the spherically symmetric logistic distribution of

$$X_{56}(x) \propto \frac{1}{1 + \exp[-\beta(x - x_{1/2})]}, \qquad (3)$$

where $x = t/t_{\rm diff}$ is a scaled depth measured from the surface to the center in units of diffusion time ($t_{\rm diff}$) of the ejecta optical depth, while β and $x_{1/2}$ are shape parameters representing the radial decline rate of the ^{56}Ni distribution and the scaled depth at which the distribution reaches half maximum, respectively. During an SN explosion, a diffusion wave travels backward into the expanding ejecta, and SN luminosities are determined by the amount of ^{56}Ni probed by the diffusion wave that reaches the center of the ejecta, or $x = 1$, some time after the SN reaches the peak luminosity.

Figure 11 (top panel) shows the early bolometric light curve (solid line) of KSP-OT-201509b predicted by the best-fit stratified ^{56}Ni distribution (Equation (3)), confirming that the stratified ^{56}Ni distribution can match the observed early bolometric luminosities (black circles) almost perfectly with the best-fit parameters $x_{1/2} = 1.0$, $\beta = 2.4$, and $t_{\rm diff} = 23.1$ days (see Figure 12 for the details of the fit). In contrast, the
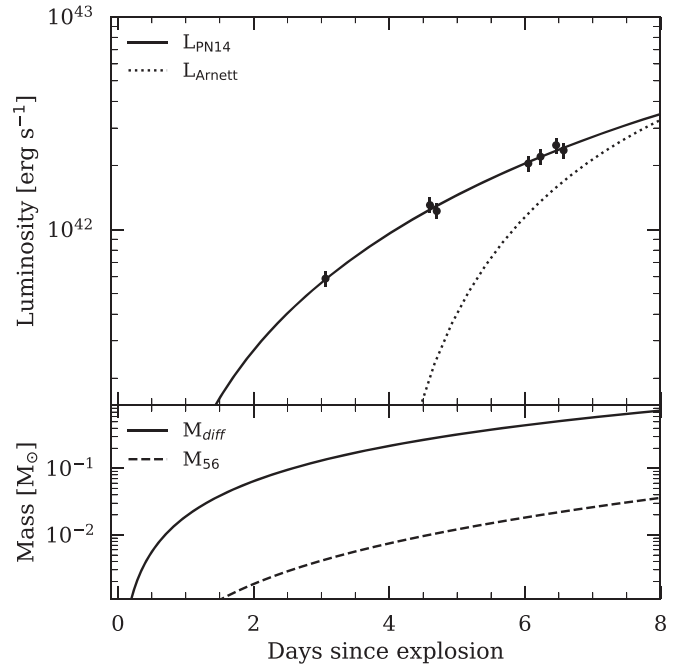

Figure 11. (Top panel) Comparison between the early bolometric luminosity light curve (black circles) of KSP-OT-201509b and the best-fit predictions ($L_{\rm PN14}$; solid line) from the model of the stratified ^{56}Ni distribution (Equation (3)) based on PN14. The error bars represent the uncertainties measured at a 68% confidence level. The dotted line is the same as the dotted black line in Figure 10, representing the luminosities extrapolated by using the best-fit parameters obtained from fitting the central part, i.e., within the interval of ± 10 days since peak, of the bolometric light curve with the model of centrally concentrated ^{56}Ni distribution in Equation (1). The abscissa is days since explosion, which is the same as the epoch of first light, in the source rest frame. (Bottom panel) Distribution of ejecta mass ($M_{\rm diff}$; solid line) and the mass of ^{56}Ni above the diffusion wave depth (M_{56}; dashed line) calculated for the best-fit stratified ^{56}Ni distribution of KSP-OT-201509b.

extrapolation of the model light curve (dotted line) based on the centrally distributed ^{56}Ni distribution from Equation (1) shows a clear underprediction. The bottom panel of the figure presents the early evolution of the estimated mass of ejecta ($M_{\rm diff}$; solid line) and ^{56}Ni (M_{56}; dashed line) above the diffusion wave (or close to the progenitor surface) where we can identify the presence of about 0.0075 $M_\odot$ ^{56}Ni mass, which corresponds to 3.4% of the ejecta, lying above the diffusion depth at 4 days. This tells us that a small amount of excess ^{56}Ni distributed shallowly can account for the early excess emission in KSP-OT-201509b, revealing that the ^{56}Ni distribution in the SN ejecta is likely more stratified toward the outer layers.

The distribution of $\chi^2_{\rm R}$ values from our model fitting of the stratified ^{56}Ni distribution, which is presented in Figure 12 as a function of $x_{1/2}$ and β, shows that the model is reasonably well fit within a curved strip of $x_{1/2} \simeq 0.4$–1.0 and $\beta \simeq 2$–5, where large $x_{1/2}$ values are paired with small β values, or vice versa. This distribution pattern of $x_{1/2}$ and β describes either a more gradually extended ^{56}Ni distribution that drops off closer to the center (= large $x_{1/2}$ and small β) or a more rapidly decaying distribution that drops off closer to the surface (= small $x_{1/2}$ and large β), both of which are consistent with a shallow ^{56}Ni distribution. The bottom panel of the figure shows the distribution of the local mass fraction of ^{56}Ni ($= X_{56}$) in two extreme cases marked in the top panel—i.e., a circle for $x_{1/2} = 1.0$ and $\beta = 2.4$ and a diamond for $x_{1/2} = 0.4$ and
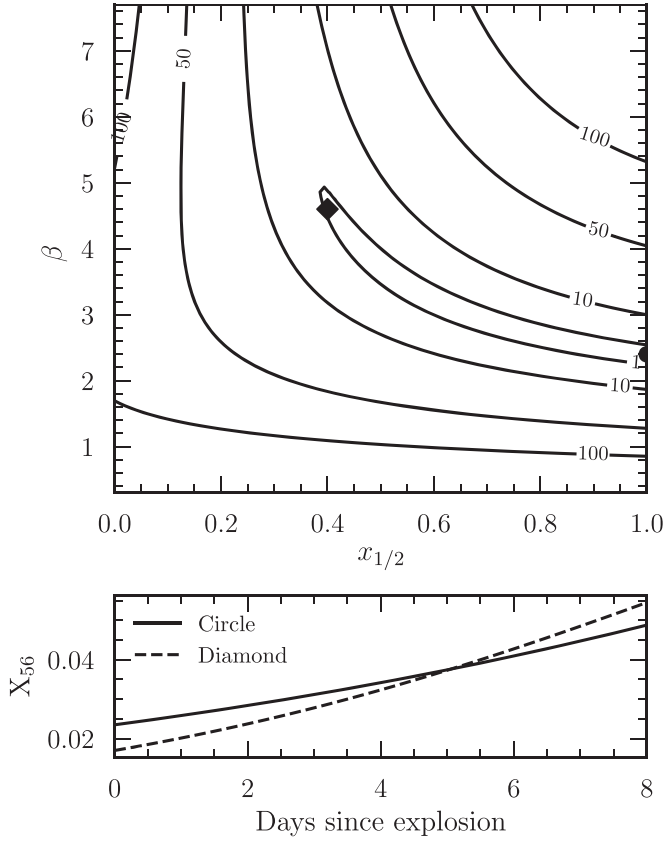
Figure 12. (Top panel) Contour plot of χ_R^2 values from the fitting of Equation (3) as a function of $x_{1/2}$, which is the scale depth where ^{56}Ni distribution is half maximum, and β, which is the decline rate of the distribution, in the model of PN14. The filled circle and diamond represent two extreme cases of $(x_{1/2}, \beta) = (1.0, 2.4)$ and $(0.4, 4.6)$, respectively. (Bottom panel) Distribution of the local mass fraction of ^{56}Ni ($= X_{56}$) for the two cases (circle and diamond) in the top panel; the solid line is for $(x_{1/2}, \beta) = (1.0, 2.4)$, and the dashed line is for $(x_{1/2}, \beta) = (0.4, 4.6)$. The abscissa is days since the epoch of explosion, which is the same as the epoch of first light, in the source rest frame.

$\beta = 4.6$—where we can confirm that both distributions require nearly the same ^{56}Ni fraction at $\sim$4–6 days after explosion.

4.2.2. Radiative Transfer Model

Magee et al. (2020) recently provided radiative transfer–based model light curves of SNe Ia with a logistic ^{56}Ni distribution using the function

$$X_{56}(m) = \frac{1}{1 + \exp[-s\,(m - M_{\mathrm{Ni}})/M_\odot]} \qquad (4)$$

for ^{56}Ni distribution, which is very similar to what is adopted in PN14 (or Equation (3) in Section 4.2.1). In this distribution, m is the mass coordinate from the ejecta surface, M_{Ni} is the total ^{56}Ni mass, and s describes how fast the ^{56}Ni distribution declines. We compare in Figure 13 the observed colors (black circles) of KSP-OT-201509b, which are binned to 1 day intervals to increase the S/Ns, during the first 10 days postexplosion to the best-fit radiative transfer models (black dashed curves; $M_{\mathrm{Ni}} = 0.4\ M_\odot$, $s = 4.4$, and $E_{\mathrm{ej}} = 0.78 \times 10^{51}$ erg) of SNe Ia from Magee et al. (2020) with Chandrasekhar-mass ejecta and exponential density distributions. The shaded gray regions in the figure represent the range of predicted colors for a set of radiative transfer models with kinetic
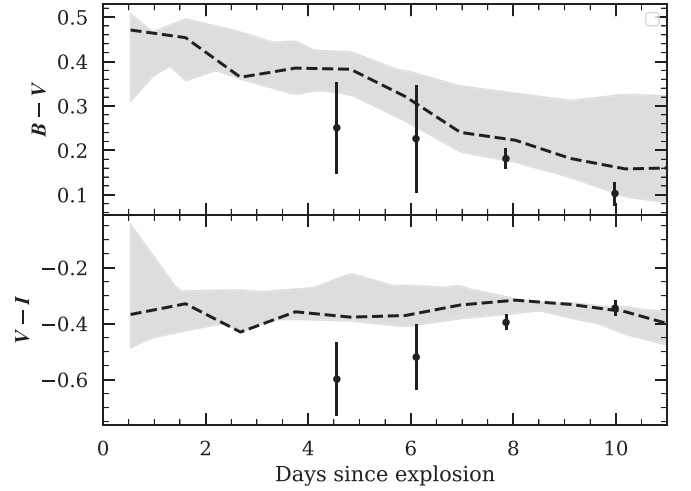

Figure 13. Comparison of the $B - V$ (top) and $V - I$ (bottom) color evolution of KSP-OT-201509b (black circles), binned to 1 day intervals to increase the S/N over the first 10 days postexplosion, to those predicted by the best-fit radiative transfer model (black dashed curves; see text) of a Chandrasekhar-mass SN Ia with logistically stratified ^{56}Ni distributions from Magee et al. (2020). The error bars represent the uncertainties measured at a 68% confidence level. The shaded gray regions show the area of the predicted colors of the models with kinetic energies in the range of $(0.5$–$2.2) \times 10^{51}$ erg for the same ^{56}Ni mass and the distribution steepness obtained from the best fit.

energies in the range of $(0.5$–$2.2) \times 10^{51}$ erg, while fixing M_{Ni} and s to those from the best fit, which are $0.4\ M_\odot$ and 4.4, respectively. We identify in the figure that the observed early color evolution of KSP-OT-201509b is largely consistent with radiative transfer–based predictions of a centrally concentrated and monotonically stratified ^{56}Ni distribution.

Magee & Maguire (2020) extended the work of Magee et al. (2020) to compute radiative transfer model light curves of Chandrasekhar-mass SNe Ia for a limited set of logistic ^{56}Ni distributions with an external shell component in the outer layers of the ejecta. In Figure 14, we compare the observed colors of KSP-OT-201509b (as in Figure 13) to the predicted light curves of the shell-added ^{56}Ni distributions of Magee & Maguire (2020). The black curve represents the best-fit model from the limited set of Chandrasekhar-mass SNe Ia with $M_{\mathrm{Ni}} = 0.6\ M_\odot$, $s = 9.7$, and $E_{\mathrm{ej}} = 1.68 \times 10^{51}$ erg for the case with no shell, while the blue, green, and red curves are for the cases of an added shell of 0.01, 0.02, and 0.03 $M_\odot$, respectively. The ^{56}Ni distribution within these shells is assumed to be a Gaussian centered at $m = 1.35\ M_\odot$ from the center of the ejecta with widths of 0.18 (solid curves) and 0.06 (dotted curves) $M_\odot$. As seen in the figure, the observed colors are less consistent with the presence of an ^{56}Ni shell of $\gtrsim 0.01\ M_\odot$ than the case of a centrally concentrated and monotonically stratified distribution of ^{56}Ni alone (Figure 13), although we cannot rule out the possibility of a thinner ^{56}Ni shell of $\lesssim 0.01\ M_\odot$ producing colors more consistent with the observations.

Overall, as shown above, the observed early color evolution of KSP-OT-201509b within the first 10 days postexplosion is consistent with what is expected from stratified, but still centrally concentrated, ^{56}Ni that extends to the shallow layers of the ejecta near the surface. The color evolution is, however, largely incompatible with the presence of a thick ($\gtrsim 0.01\ M_\odot$), external shell component of ^{56}Ni in addition to the logistic distribution. This indicates that if KSP-OT-201509b originated in a sub-Ch explosion triggered by an He-shell detonation
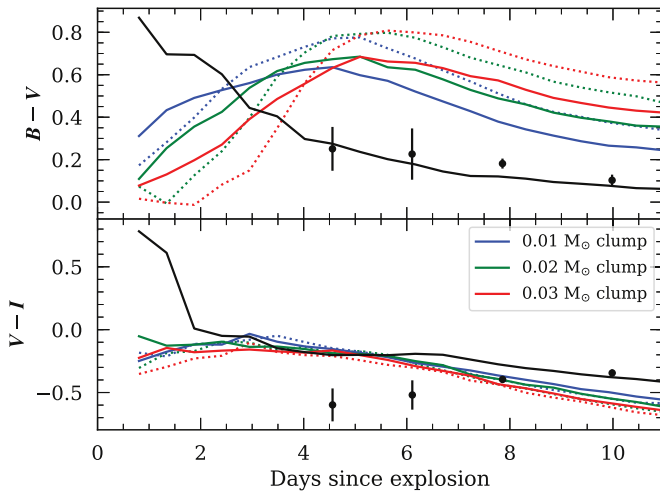
Figure 14. Same $B - V$ (top) and $V - I$ (bottom) colors (black circles) of KSP-OT-201509b as in Figure 13 but compared to the radiative transfer model light curves (colored curves) of Magee & Maguire (2020) for a Chandrasekhar-mass SN Ia with a logistically stratified ^{56}Ni distribution and an external shell component (see text). The solid blue, green, and red curves represent the cases with a shell of 0.01, 0.02, and 0.03 $M_\odot$, respectively. The solid curves are for a shell width of 0.18 $M_\odot$, whereas the dotted curves are for 0.06 $M_\odot$. The black solid curve represents the case with no external shell.

process (e.g., Kromer et al. 2010), a thinner shell would have been required, such as recently shown in simulations of He-shell detonations with thin, enriched He shells (e.g., Townsley et al. 2019).

5. Constraint on the Progenitor of KSP-OT-201509b

The high-cadence, multicolor light curves of KSP-OT-201509b (Figure 2) provide a rare opportunity to place thorough constraints on the progenitors of rapidly declining SNe Ia of a transitional nature. For an SN Ia from a single-degenerate progenitor system composed of a WD and either a main-sequence (MS) subgiant or a red giant companion, Kasen (2010; see also Boehner et al. 2017) calculated model luminosities from the shock interactions between the SN ejecta and the companion that are mainly determined by the mass, kinetic energy, and opacity of the ejecta, as well as by the progenitor binary separation distance. Such emission has been discussed as the source of early flashes within roughly 5 days postexplosion in SNe Ia (e.g., Miller et al. 2018, 2020). The observable luminosity from the interaction can be approximated by $L_{int}(t)f(\theta)$, where $L_{int}(t)$ is the intrinsic luminosity from the interaction at time t, and $f(\theta) = 0.982 \exp[-(\theta/99.7)^2] + 0.018$ is the distribution of the observed luminosity as a function of the viewing angle θ (Olling et al. 2015). The maximum observable luminosity occurs when an SN is viewed along the interaction axis from the side of the companion, or $\theta = 0°$.

Figure 15 compares the observed BVI magnitudes (black plus signs) and limiting magnitudes (black inverted triangles) of the KSP-OT-201509b light curve from its early phase with those expected by the ejecta and companion interaction model (Kasen 2010) for three particular companion cases of 1RG (blue line), 6MS (orange line), and 2MS (green line) when viewed along the interaction axis from the companion side. These three cases are for progenitor systems where the Roche lobe–filling companion is a red giant of 1 $M_\odot$ (1RG), an MS subgiant of 6 $M_\odot$ (6MS), and 2 $M_\odot$ (2MS) located at 2×10^{13},
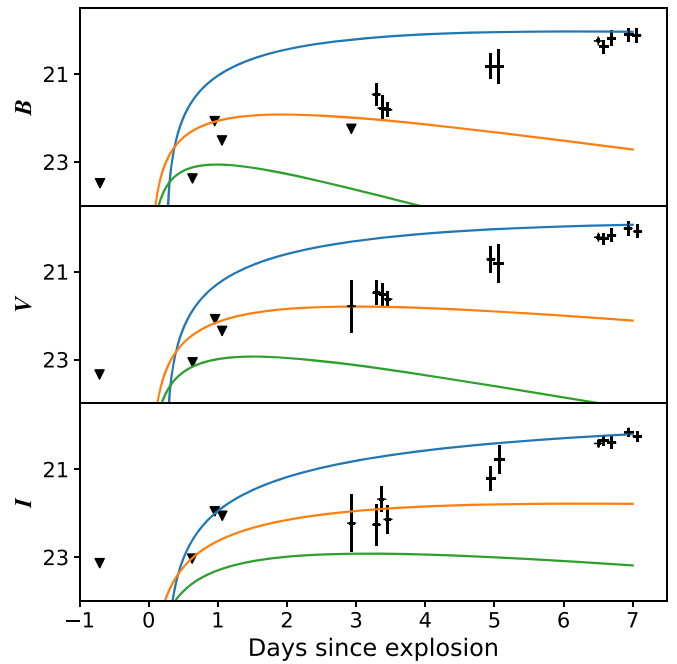

Figure 15. Comparison between the observed BVI magnitudes of KSP-OT-201509b and those expected by Kasen (2010) for the interaction between the ejecta and the companion when viewed along the interaction axis from the companion side. The abscissa is days since the epoch of explosion, which is the same as the epoch of first light ($= t_0$) in the source rest frame; the ordinates are BVI magnitudes (from top to bottom). The black plus signs represent the observed magnitudes, with the vertical extensions corresponding to the uncertainties measured at a 95% confidence level. In order to increase the depth of the measurements, we combine about five nearby individual exposures distributed within a time span of 2 ± 1 hr. The black inverted triangles are detection limits at S/N $= 2$, which ranges between 22nd and 24th magnitude depending on the quality of the binned images. The three solid lines represent model expectations for the 1RG (blue), 6MS (orange), and 2MS (green) cases by Kasen (2010).

2×10^{12}, and 5×10^{11} cm, respectively, from the WD. We use the estimated parameters of KSP-OT-201509b in Table 2 and ejecta opacity $\kappa = 0.2 \, \mathrm{cm}^2 \, \mathrm{g}^{-1}$ attributed to electron scattering (Kasen 2010) to estimate luminosities from the interaction (L_{int}) between the ejecta and companion. As in the figure, the observed BVI-band brightnesses (including the upper limits) of KSP-OT-201509b are lower than what is predicted by the interactions between the companion and ejecta in the 1RG case (blue line) in most of the observed epochs, and this is also true for the case of 6MS (orange line) at the epochs earlier than day 3. This comparison shows that both the 1RG and 6MS models are incompatible with the observations, since the observed fluxes need to be larger than the model predictions to allow for the presence of emission from the ejecta–companion interactions. The 2MS case (green line) is different from the 1RG and 6MS cases because only the B-band brightness obtained around 0.6 day is lower than the model prediction, while all other observed brightnesses (including the upper limits) are higher. The 2MS case, therefore, still appears to be incompatible with the model prediction, but with less confidence than the 1RG and 6MS cases. In conclusion, if the interactions between the ejecta and the binary companions are indeed viewed along the interaction axis from the companion side in KSP-OT-201509b, our comparisons show that the companion of the source was located in closer proximity to the WD than the 1RG and 6MS cases, and likely the 2MS case too, indicating that the size of the progenitor companion of KSP-OT-201509b is smaller than

those of these three stars. We now provide a much more thorough and general investigation into the presence of potential emission originating from the ejecta–companion interactions and conclude that it is highly likely that the companion of KSP-OT-201509b was a WD, supporting the double-degenerate scenario.

We first expand our search for the signal from the potential interactions between the ejecta and companion in KSP-OT-201509b by including an extensive set of companion types, far beyond the 1RG, 2MS, and 6MS cases, for all possible oblique viewing angles, i.e., $\theta > 0°$, and also by fully accounting for the uncertainties in our photometric measurements. For this, we choose a set of 60 distances in the range of $(0.001–10) \times 10^{13}$ cm in logarithmic scale as trial binary separation distances of the progenitor. This range of separation distances corresponds to that of the Roche radius separations of stars from the smallest red dwarfs to the largest supergiants. We then calculate predicted brightnesses from the ejecta–companion interaction in BVI with these separation distances using the model of Kasen (2010) for a set of 100 viewing angles equally sampled in the range of $\theta = 0°–180°$. In this process, we compare the predicted brightnesses to the observed light curves at various confidence levels by adopting a Gaussian distribution of the observed BVI magnitudes (including the upper limits; Figure 15) of the source with their photometric uncertainties. Figure 16 shows our results, where the abscissa is the binary separation distance and the ordinate represents the lower limit of acceptable viewing angles for the interaction between the ejecta and its companion in KSP-OT-201509b based on the model of Kasen (2010) at confidence levels of 68% (solid curve) and 95% (dashed curve). At the 95% confidence level (dashed curve), as in the figure, only highly oblique viewing angles $\theta \gtrsim 130°$ are allowed for separation distances larger than 2×10^{13} cm, whereas all of the small viewing angles are ruled out. For small separation distances of $<0.03 \times 10^{13}$ cm, on the other hand, we cannot rule out any viewing angles. In the separation distance range of $(0.03–2) \times 10^{13}$ cm, the lower limit of acceptable viewing angles increases along the separation distance, ruling out more viewing angles for larger separation distances. At the 68% confidence level (solid curve), they are naturally more constrained than the 95% case (dashed curve); almost all viewing angles are excluded for large separation distances, while we cannot rule out any angle only for separation distances smaller than 0.007×10^{13} cm.

The results shown in Figure 16 accommodate the photometric uncertainties of the light curves of KSP-OT-201509b but not those of the estimated values of the redshift, epoch of first light, and ejecta mass and kinetic energy needed to compute the model luminosities from the ejecta–companion interactions. In order to reflect the uncertainties of those parameters in our analyses, we conduct 40,000 Monte Carlo simulations of the light curves of the ejecta–companion interactions predicted by Kasen (2010) by randomly selecting the values of these parameters under the assumption that they follow a Gaussian distribution with the measured uncertainties. We use the same set of separation distances and viewing angles that we used above for Figure 16 and then conduct a comparison between the observed light curves of KSP-OT-201509b with the model light curves. Figure 17 shows the results of our comparison, wherein all of the viewing angles are allowed for the separation distances up to $\simeq 0.045 \times 10^{13}$ cm at a confidence level of 95% when all of the uncertainties are statistically accounted for. The separation distance of
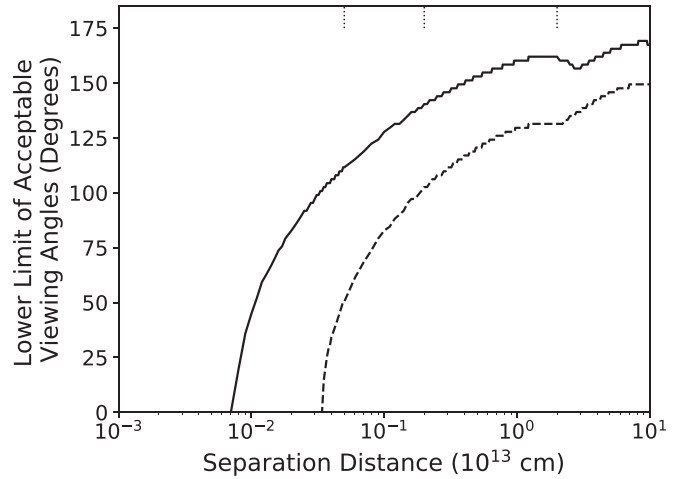

Figure 16. Lower limit of acceptable viewing angles for the interaction between KSP-OT-201509b and its potential companion predicted by Kasen (2010) as a function of separation distance, i.e., Roche radius separation, in units of 10^{13} cm for two confidence levels of 68% (solid line) and 95% (dashed line) obtained by taking the photometric measurement uncertainties into account statistically (see text). The three dotted vertical lines in the upper y-axis represent the separation distances for the 2MS, 6MS, and 1RG cases at 0.05×10^{13}, 0.2×10^{13}, and 2×10^{13} cm, respectively. The nonsmooth feature at large separation distances is a result of the uneven quality of our data obtained at different epochs.

0.045×10^{13} cm is about 90% of that of 2MS, after which the lower limit of the acceptable viewing angle increases. At separation distances larger than that of 1RG, only large viewing angles, i.e., $\theta > 125°$, are allowed. The constraints on the viewing angles become more stringent at the 68% confidence level, with even small viewing angles being ruled out at very short separation distances.

Our analyses above apparently show that there is not much chance for the companion of KSP-OT-201509b to have been a red giant, considering that the lower limit of the acceptable viewing angles rules out most of the viewing angles for such a large star. Note that it is highly unlikely that the companion was at a different location from the Roche radius separation, where it can provide the stable accretion needed to trigger the explosion. An MS subgiant appears to be more probable than the red giant in our analyses, especially at highly oblique viewing angles; however, sustaining substantial accretion from such an MS companion for an SN Ia detonation is more challenging. These results indicate that a double-degenerate system is much more likely to have been the progenitor system of KSP-OT-201509b, which agrees well with the results of the statistical searches for ejecta–companion shock interactions in the surveys of the Sloan Digital Sky Survey, SNLS, and TESS (Hayden et al. 2010; Bianco et al. 2011; Fausnaugh et al. 2021), as well as those of individual SN studies of SN 2011fe (Li et al. 2011a; Nugent et al. 2011), SN 2012ht (Yamanaka et al. 2014), SN 2013gy (Holmbo et al. 2019), ASASSN-14lp (Shappee et al. 2016), and SN 2012cg (Shappee et al. 2018; although see Marion et al. 2016), strengthening the case for small companions for the majority of SN Ia progenitors (e.g., Olling et al. 2015). However, we also note that some SNe, e.g., SN 2014J (Goobar et al. 2015), SN 2017cbv (Hosseinzadeh et al. 2017), and SN 2018oh (Dimitriadis et al. 2019; Shappee et al. 2019), do show indications of early excess emission that could come from ejecta–companion shock interactions, although it is possible that some other processes—such as
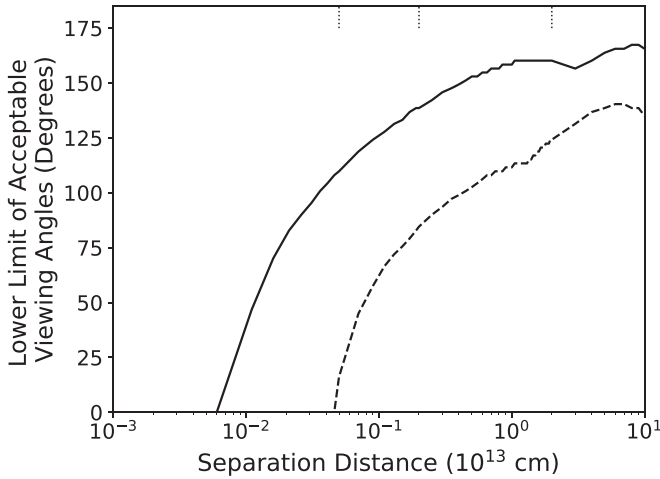
Figure 17. Same as Figure 16 but for the confidence levels (solid line for 68%, dashed line for 95%) obtained from 40,000 Monte Carlo simulations of the model luminosities from ejecta–companion interactions (Kasen 2010). The luminosities are computed by randomly selecting the values of a comprehensive set of the observed and estimate parameters (including redshift, ejecta mass and kinetic energy, epoch of first light, and photometric measurements) of KSP-OT-201509b under the assumption that their uncertainty distributions are Gaussian.

circumstellar interactions or shallow layers of ^{56}Ni—are responsible for it.

6. Missing Host Galaxy for KSP-OT-201509b

As shown in Figure 1 (see also Section 2), no host galaxy underlying KSP-OT-201509b is detected in our deep stack images reaching sensitivity limits of $\simeq 27.8$ (B), 28.5 (V), and 28.2 (I) mag arcsec^{-2}, while source G, which is the only apparently extended source near KSP-OT-201509b, is located $\sim 27''$ away in the southwestern direction. In order to understand the nature of G and its potential connection to KSP-OT-201509b, we fit its V-band surface brightness with the Sérsic profile $\mu = \mu_0 + 1.0857\, b_n (r/r_e)^{1/n}$ (where μ_0, r, r_e, and n are the central surface brightness, radius, effective radius, and Sérsic curvature index, respectively, and $b_n = 1.9992n{-}0.3271$; see Graham & Driver 2005) to obtain $\mu_0 = 19.04 \pm 0.14$ mag arcsec^{-2}, $r_e = 3''63 \pm 0''03$, and $n = 2.05 \pm 0.06$. The apparent V-band magnitude and $B - V$ color of G are $V \simeq 17.38$ and $B - V \simeq 1.4$ mag, respectively. These fitted parameters and the color of G are similar to those found in early-type galaxies (Valentinuzzi et al. 2011; Bassett et al. 2013), which is consistent with its spectroscopic properties. Figure 18 shows our Magellan spectrum of G (see Section 2 for the details of the observations) with clear detections of Ca H + K, G, and Na I D absorption lines, typical of early-type galaxies. We determine the redshift of G to be $z \simeq 0.167 \pm 0.001$ using the measured wavelengths of the absorption lines, where the uncertainty is due to the rms wavelength solution error of 0.135 Å. The measured redshift is much larger than the $z = 0.072 \pm 0.003$ inferred for KSP-OT-201509b by fitting to an SN Ia template (Section 3.3). Figure 19 compares the best-fit SNooPy Branch-normal template (dotted curve) obtained at $z = 0.167$ with those in Figure 7, clearly showing that it gives significantly worse results than the fit obtained at $z = 0.072$. In addition, in order for KSP-OT-201509b to be an SN Ia with a high redshift of $z = 0.167$, its observed B-band peak brightness requires the SN to have either a peculiar motion greater than 14,000 km s^{-1} or a
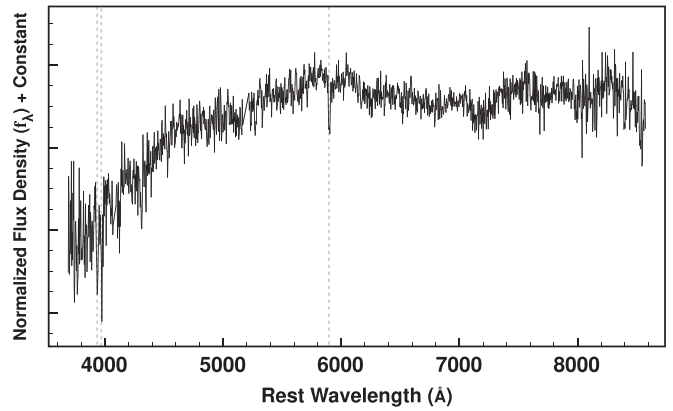

Figure 18. Spectrum of the nearby galaxy G obtained with the Magellan telescope. Absorption lines of Ca II H + K and Na I D are marked by dashed vertical lines. Their wavelengths are consistent with the redshift $z = 0.167 \pm 0.001$ for the galaxy G.
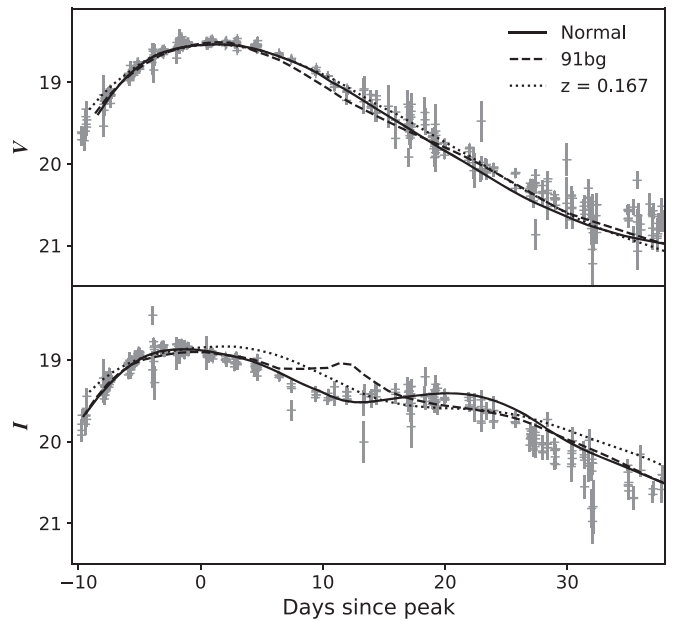

Figure 19. Same as Figure 7 but with the dotted lines representing the best SNooPy template fits of KSP-OT-201509b with $z = 0.167$.

peak absolute magnitude more luminous than -21.8 mag with $\Delta M_{B,15} \simeq 1.96$ mag. Both of these are unrealistic, since the required peculiar motion is more than 20 times greater than what can be expected for the source (see Section 3.3), and the required peak luminosity and $\Delta M_{B,15}$ make the source an extremely luminous SN Ia with an exceptionally large decline rate. We therefore conclude that G is unrelated to KSP-OT-201509b and is an early-type galaxy located at a much larger redshift. This leaves KSP-OT-201509b still hostless.

In order to investigate whether another nearby detected source may be the host galaxy of KSP-OT-201509b, we then calculate the probability that 22 sources identified within about $35''$ from KSP-OT-201509b in our deep BVI images with $S/N > 2$ are random galaxies coincidentally located in the field by adopting the methodology in Bloom et al. (2002) using their magnitudes and distances from KSP-OT-201509b (see also Berger 2010, and details therein). In Figure 20, which shows the calculated probabilities of chance coincidence as a function of distance, all sources have a high (>0.4) chance of
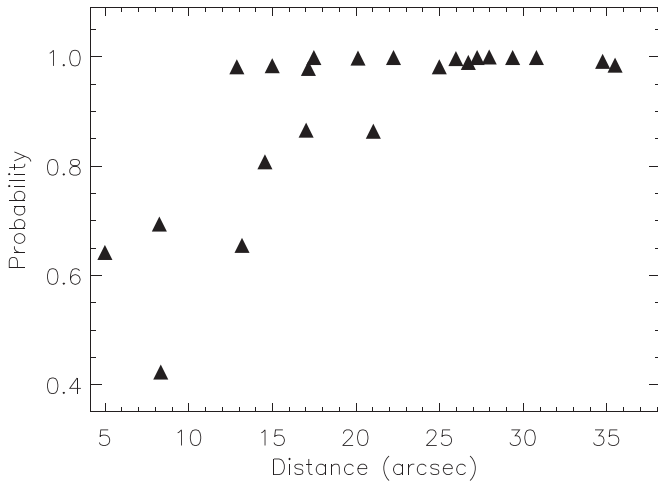
Figure 20. Probability of chance coincidence of the 22 closest sources (excluding the galaxy G) identified in our deep *BVI* images as a function of distance from KSP-OT-201509b.

coincidence probabilities, with the majority near 1. This tells us that all of these sources near KSP-OT-201509b are likely to be coincident by chance and unlikely to be related to the SN.

The absence of any host galaxy candidate of KSP-OT-201509b in our deep stack images hints at the nature of its host galaxy, since, at a luminosity distance of $\simeq$310 Mpc (or $z \simeq 0.072$), regular galaxies should be easily identifiable as an extended object (see Agulli et al. 2014, for example) in our images. Considering that there is no such extended object other than G, which is at a much higher redshift, in the vicinity of KSP-OT-201509b, it is highly likely that the host galaxy of KSP-OT-201509b is a faint dwarf galaxy. The limiting magnitudes of an unresolved source in our images are $B \simeq 25.83$, $V \simeq 25.30$, and $I \simeq 24.74$ mag. This corresponds to an absolute magnitude limit of $\simeq -12$ mag in the V band at $z = 0.072$ and is compatible with the previously known V-band absolute magnitude range of dwarf galaxies (Tolstoy et al. 2009). The nearest unresolved source to KSP-OT-201509b in Figure 1 is about 5″ away from KSP-OT-201509b with V- and I-band magnitudes of 24.14 ± 0.15 and 23.99 ± 0.17 mag, respectively. If this unresolved source is a dwarf galaxy hosting KSP-OT-201509b, the SN is located $\sim$6.6 kpc away from the center of the host galaxy. Its V-band absolute magnitude is -13.23 mag at $z = 0.072$, and a dwarf galaxy with such a magnitude is expected to have $\simeq 25$ mag arcsec^{-2} effective surface brightness and $\simeq 1$ kpc effective radius (Tolstoy et al. 2009; Conroy & Bullock 2015). This requires KSP-OT-201509b to have exploded at a location away from the center of a dwarf galaxy more than six times its effective radius. According to Kravtsov (2013), the stellar density in a dwarf galaxy at such a location drops significantly more than, i.e., $\gg$50 times, the central part. We therefore conclude again that it is highly unlikely that any source identified in our deep stack images is the host galaxy of KSP-OT-201509b and that the host galaxy of the SN is most likely a dwarf galaxy fainter than our detection limit. The inferred insignificant host galaxy extinction of KSP-OT-201509b (Sections 2 and 3.2) points to the outskirts of its potential host galaxy as the explosion location.

Recently, there has been a growing number of SNe Ia detected in low-luminosity dwarf galaxies, as well as those that remained hostless. These include (1) SN 1999aw, a luminous and slow-

decaying SN from a very faint galaxy with $M_V = -12.4$ mag (Strolger et al. 2002); (2) SN 2007qc, from an extremely faint host galaxy with $M_B \sim -11$ mag (Quimby et al. 2012); (3) SN 2007if, a luminous super-Chandrasekhar-mass SN Ia detected in a host galaxy with $M_g = -14.45$ mag (Childress et al. 2011); and (4) PTF 10ops, a peculiar-type SN with subluminous spectral properties but a normal light-curve width that remains hostless to the detection limit of $r \gtrsim -12$ mag (Maguire et al. 2011). It is also noteworthy that the group of Ca-rich transients, whose thermonuclear origin is still under debate, have consistently been found in the outskirts of their host galaxies where there is no apparent stellar population, preferring high-velocity progenitors to low-metallicity environments (Yuan et al. 2013; Foley 2015; Lyman et al. 2016; Lunnan et al. 2017). Graham et al. (2015) identified the host of an SN Ia with $M_V \simeq -8.4$ mag, which may be either a dwarf galaxy or a globular cluster from a nearby elliptical galaxy, along with two other cases where no host galaxy is identified to the limit of $M_R > -9.2$ mag, suggesting that their progenitors most likely belong to the intracluster stellar population. Although SNe Ia from a faint host, including those from the intracluster environment and dwarf galaxies, can potentially bring us important insight into the connection between their progenitors and stellar population and be used to trace missing dwarf galaxies in the local universe (e.g., Conroy & Bullock 2015; Graham et al. 2015), our understanding of such SNe Ia is still highly incomplete, mainly due to the lack of a statistically meaningful sample size. The identification of KSP-OT-201509b as a rapidly declining hostless SN Ia of a transitional nature indicates that this type of SN Ia can be produced in faint dwarf galaxies and that the coupling between specific types of SN Ia and host galaxy environment may not be as strong as previously thought, considering that the transitional SNe Ia have largely been detected in early-type galaxies (e.g., Mazzali et al. 2007; Ashall et al. 2016).

7. Summary and Conclusion

In this paper, we report the discovery and identification of KSP-OT-201509b as a rapidly declining hostless SN Ia of a transitional nature likely originating from a sub-Ch explosion in a double-degenerate progenitor based on high-cadence, multicolor observations made with the KMTNet. We summarize our results and conclusions as follows.

1. The observed light curves and colors of KSP-OT-201509b are compatible with a rapidly declining SN Ia at $z \simeq 0.072$ whose properties are intermediate between Branch-normal and 91bg-like but much closer to the former, with clear signs of a transitional nature. While the evolution of its early light curves is well fitted with a power law representing a homologous expansion powered by ^{56}Ni radioactive decay that is mediated by photon diffusion processes, the overall $B - V$ and $V - I$ color evolution of KSP-OT-201509b is largely synchronous with that of the I band, as found in other SNe Ia. We identify the presence of an early redward evolution in the $V - I$ color prior to -10 days since peak in the SN before it enters the previously known phase of blueward evolution. This early redward evolution in $V - I$ has not been studied much but may bear an important clue to understanding the physical conditions of SN explosions.

2. The Phillips and color stretch parameters of KSP-OT-201509b are $\Delta M_{B,15} = 1.62 \pm 0.03$ mag and $s_{BV} = 0.54 \pm 0.05$, respectively, which places the source in the gap

between the two groups of Branch-normal and 91bg-like with a peak luminosity of $(9.0 \pm 0.3) \times 10^{42}$ erg s^{-1}. The transitional nature of the source is also confirmed with the relative strength ($\simeq 0.309$) of the secondary I-band peak of the source and its $B - V \simeq 0.08$ mag color at the peak epoch. We obtain $M_{\mathrm{Ni}} = 0.32 \pm 0.01\ M_\odot$, $M_{\mathrm{ej}} = 0.84 \pm 0.12\ M_\odot$, and $E_{\mathrm{ej}} = (0.61 \pm 0.14) \times 10^{51}$ erg, which makes KSP-OT-201509b an SN Ia explosion with a sub-Ch mass.

3. The bolometric light curve of KSP-OT-201509b shows the presence of early excess emission to what is expected from a centrally concentrated ^{56}Ni distribution. We find that a stratified ^{56}Ni distribution extended more shallowly to the surface of the progenitor provides a good match to the observed bolometric light curve, while the presence of a thick, $\gtrsim 0.01\ M_\odot$, external shell is largely incompatible with the observed early color evolution. Thorough comparisons between the observed light curves and those predicted from the ejecta–companion interactions clearly prefer a small binary separation distance for the progenitor, favoring the double-degenerate scenario for its origin.

4. Even in our deep stack images reaching the sensitivity limit $\mu_{BVI} \simeq 28$ mag arcsec^{-2}, KSP-OT-201509b remains hostless, suggesting that its host galaxy is a faint dwarf galaxy. This contradicts what has been previously thought for the types of host galaxies that produce transitional SNe Ia. It will be worthwhile to investigate the nature of the host galaxy of KSP-OT-201509b with deeper imaging observations than presented in this paper that can provide new insight into the relationship between host galaxies and types of SNe Ia.

Facilities: KMTNet, Magellan, AAVSO.

Software: Astropy (Astropy Collaboration et al. 2013, 2018), SNooPy (Burns et al. 2011), SCAMP (Bertin 2006), SWARP (Bertin et al. 2002), SiFTO (Conley et al. 2008).

ORCID iDs

Dae-Sik Moon ⓘ https://orcid.org/0000-0003-4200-5064
Yuan Qi Ni ⓘ https://orcid.org/0000-0003-3656-5268
Maria R. Drout ⓘ https://orcid.org/0000-0001-7081-0082
Santiago González-Gaitán ⓘ https://orcid.org/0000-0001-9541-0317
Niloufar Afsariardchi ⓘ https://orcid.org/0000-0002-1338-490X
Hong Soo Park ⓘ https://orcid.org/0000-0002-3505-3036
Youngdae Lee ⓘ https://orcid.org/0000-0002-6261-1531
Sang Chul Kim ⓘ https://orcid.org/0000-0001-9670-1546
John Antoniadis ⓘ https://orcid.org/0000-0003-4453-3776
Dong-Jin Kim ⓘ https://orcid.org/000-0002-4292-9649
Yongseok Lee ⓘ https://orcid.org/0000-0001-7594-8072

References

Afsariardchi, N., Moon, D.-S., Drout, M. R., et al. 2019, ApJ, 881, 22
Agulli, I., Aguerri, J. A. L., Sanchez-Janssen, R., et al. 2014, MNRAS, 444, 34
Ahsall, C., Mazzali, P. A., Stritzinger, M. D., et al. 2018, MNRAS, 477, 153
Arnett, D. W. 1982, ApJ, 253, 785
Arnett, D. W. 1996, Nucleosynthesis and Supernovae (Princeton, NJ: Princeton Univ. Press)
Ashall, C., Mazzali, P. A., Pian, E., & James, P. A. 2016, MNRAS, 463, 1891
Ashcraft, T. A., Windhorst, R. A., Jansen, R. A., et al. 2018, PASP, 130, 064102
Astropy Collaboration, Price-Whelan, A. M., Sipőcz, B. M., et al. 2018, AJ, 156, 123
Astropy Collaboration, Robitaille, T. P., Tollerud, E. J., et al. 2013, A&A, 558, A33
Bassett, R., Papovich, C., Lotz, J. M., et al. 2013, ApJ, 770, 58
Berger, E. 2010, ApJ, 772, 1946
Bertin, E. 2006, in ASP Conf. Ser. 351, Astronomical Data Analysis Software and Systems XV, ed. C. Gabriel et al. (San Francisco, CA: ASP), 112
Bertin, E., Mellier, Y., Radovich, M., et al. 2002, in ASP Conf. Ser. 281, Astronomical Data Analysis Software and Systems XI, ed. D. A. Bohlender, D. Durand, & T. H. Handley (San Francisco, CA: ASP), 228
Bianco, F. B., Howell, D. A., Sullivan, M., et al. 2011, ApJ, 741, 20
Blondin, S., Dessart, L., Hillier, J., & Khokhlov, A. M. 2017, MNRAS, 470, 157
Bloom, J. S., Kulkarni, S. R., & Djorgovski, S. G. 2002, AJ, 123, 1111
Boehner, P., Plewa, T., & Langer, N. 2017, MNRAS, 465, 2060
Boubert, D., Erkal, D., Evans, N. M., & Izzard, R. G. 2017, MNRAS, 469, 2151
Brown, W. R. 2015, ARA&A, 53, 15
Burns, C. R., Parent, E., Phillips, M. M., et al. 2018, ApJ, 869, 56
Burns, C. R., Stritzinger, M., Phillips, M. M., et al. 2011, AJ, 141, 19
Burns, C. R., Stritzinger, M., Phillips, M. M., et al. 2014, ApJ, 789, 32
Childress, M., Aldering, G., Aragon, C., et al. 2011, ApJ, 733, 3
Conley, A., Sullivan, M., Hsiao, E. Y., et al. 2008, ApJ, 681, 482
Conroy, C., & Bullock, J. S. 2015, ApJL, 805, L2
Contardo, G., Leibundgut, B., & Vacca, W. D. 2000, A&A, 359, 876
Contreras, C., Hamuy, M., Phillips, M. M., et al. 2010, AJ, 139, 519
Contreras, C., Phillips, M. M., Burns, C. R., et al. 2018, ApJ, 859, 24
Dhawan, S., Bulla, M., Goobar, A., et al. 2018, MNRAS, 480, 1445
Dhawan, S., Leibundgut, B., Spyromilio, J., & Blondin, S. 2017, A&A, 602, A118
Dhawan, S., Leibundgut, B., Spyromilio, J., & Maguire, K. 2015, MNRAS, 448, 1345
Dimitriadis, G., Foley, R. J., Rest, A., et al. 2019, ApJL, 870, L1
Drinkwater, M. J., Gregg, M. D., & Colless, M. 2001, ApJ, 548, 139
Fausnaugh, M. M., Vallely, P. J., Kochanek, C. S., et al. 2021, ApJ, 908, 51
Filippenko, A. V., Richmond, M. W., Branch, D., et al. 1992, AJ, 104, 1543
Foley, R. J. 2015, MNRAS, 452, 2463
Gall, C., Stritzinger, M. D., Ashall, C., et al. 2018, A&A, 611, 33
Goldstein, D. A., & Kasen, D. 2018, ApJL, 852, L33
González-Gaitán, S., Perrett, K., Sullivan, M., et al. 2011, ApJ, 727, 107
Goobar, A., Kromer, M., Siverd, R., et al. 2015, ApJ, 799, 106
Graham, A. W., & Driver, S. P. 2005, PASA, 22, 118
Graham, M. L., Sand, D. J., Zaritsky, D., & Pritchet, C. J. 2015, ApJ, 807, 83
Guy, J., Astier, P., Baumont, S., et al. 2007, A&A, 466, 11G
Hamuy, M., Phillips, M. M., Suntzeff, N. B., et al. 1996, AJ, 112, 2438
Hayden, B. T., Garnavich, P. M., Kasen, D., et al. 2010, ApJ, 722, 1691
Hoeflich, P., Hsiao, E. Y., Ashall, C., et al. 2017, ApJ, 846, 58
Holmbo, S., Stritzinger, M. D., Shappee, B. J., et al. 2019, A&A, 627, A174
Hosseinzadeh, G., Sand, D. J., Valenti, S., et al. 2017, ApJL, 845, L11
Howell, D. A. 2001, ApJL, 554, L193

Hoyle, F., & Fowler, W. A. 1960, ApJ, 132, 565
Hsiao, E. Y., Burns, C. R., Contreras, C., et al. 2015, A&A, 578, A9
Iben, I., Jr., & Tutukov, A. V. 1984, ApJS, 54, 335
Kasen, D. 2006, ApJ, 649, 939
Kasen, D. 2010, ApJ, 708, 1024
Kim, S.-L., Lee, C.-U., Park, B.-G., et al. 2016, JKAS, 49, 37
Kravtsov, A. V. 2013, ApJL, 764, L31
Krisciunas, K., Phillips, M. M., Stubbs, C., et al. 2001, AJ, 122, 1616
Kromer, M., Sim, S. A., Fink, M., et al. 2010, ApJ, 719, 1067
Leibundgut, B., Kirshner, R. P., Phillips, M. M., et al. 1993, AJ, 105, 301
Lewis, G. F., Ibata, R. A., Chapman, S. C., et al. 2007, MNRAS, 375, 1364
Li, W., Bloom, J. S., Podsiadlowski, P., et al. 2011a, Natur, 480, 348
Li, W., Filippenko, V., Riess, A. G., Hu, J., & Qiu, Y. 2001, ApJ, 546, 734
Li, W., Leaman, J., Chornock, R., et al. 2011b, MNRAS, 412, 1441
Li, W., Wang, X., Vinkó, J., et al. 2019, ApJ, 870, 12
Lunnan, R., Kasliwal, M. M., Cao, Y., et al. 2017, ApJ, 836, 60
Lyman, J. D., Levan, A. J., James, P. A., et al. 2016, MNRAS, 458, 1768
Magee, M. R., & Maguire, K. 2020, A&A, 642, 189
Magee, M. R., Maguire, K., Kotak, R., et al. 2020, A&A, 634, 37
Maguire, K., Sullivan, M., Thomas, R. C., et al. 2011, MNRAS, 418, 747
Marion, G. H., Brown, P. J., Hsiao, E. Y., et al. 2016, ApJ, 820, 92
Mazzali, P. A., Röpke, F. K., Benetti, S., & Hillebrandt, W. 2007, Sci, 315, 825
Miller, A. A., Cao, Y., Piro, A. L., et al. 2018, ApJ, 852, 100
Miller, A. A., Magee, R. R., Polin, A., et al. 2020, ApJ, 898, 56
Moffat, A. F. J. 1969, A&A, 3, 455
Moon, D.-S., Kim, S. C., Lee, J.-J., et al. 2016, Proc. SPIE, 9906, 99064I
Nugent, P. E., Sullivan, M., Cenko, S. B., et al. 2011, Natur, 480, 344
Olling, R. P., Mushotzky, R., Shaya, E. J., et al. 2015, Natur, 521, 332
Palanque-Delabrouille, N., Ruhlmann-Kleider, V., Pascal, S., et al. 2010, A&A, 514, A63
Park, H. S., Moon, D.-S., Zaritsky, D., et al. 2017, ApJ, 848, 19
Park, H. S., Moon, D.-S., Zaritsky, D., et al. 2019, ApJ, 885, 88
Parrent, J., Friesen, B., & Parthasarathy, M. 2014, Ap&SS, 351, 1
Parrent, J., Howell, D. A., Friesen, B., et al. 2012, ApJL, 752, L26
Patat, F., Benetti, S., Cappellaro, I. J., et al. 1996, MNRAS, 278, 111
Pereira, R., Thomas, R. C., Aldering, G., et al. 2013, A&A, 544, 27
Phillips, M. M. 1993, ApJL, 413, L105

Phillips, M. M., Lari, P., Suntzeff, N. B., et al. 1999, AJ, 118, 1766
Phillips, M. M., Phillips, A. C., Heathcote, S. R., et al. 1987, PASP, 99, 592
Pinto, P. A., & Eastman, R. G. 2000, ApJ, 530, 757
Piro, A., & Nakar, E. 2014, ApJ, 784, 85
Piro, A. L., & Morozava, V. S. 2016, ApJ, 826, 96
Prieto, J. L., Rest, A., Suntzeff, N. B., et al. 2006, ApJ, 647, 501
Quimby, R. M., Yuan, F., Akerlof, C., Wheeler, J. C., & Warren, M. S. 2012, AJ, 144, 17
Riess, A. G., Macri, L. M., Hoffmann, S. L., et al. 2016, ApJ, 826, 56
Scalzo, R. A., Parent, E., Burns, C., et al. 2019, MNRAS, 483, 628
Schlafly, E. F., & Finkbeiner, D. P. 2011, ApJ, 737, 103
Schlegel, D. J., Finkbeiner, D. P., & Davis, M. 1998, ApJ, 500, 525
Shappee, B. J., Holoien, T. W.-S., Drout, M. R., et al. 2019, ApJ, 870, 13
Shappee, B. J., Piro, A. L., Stanek, K. Z., et al. 2016, ApJ, 826, 144
Shappee, B. J., Piro, A. L., Stanek, K. Z., et al. 2018, ApJ, 855, 6
Spergel, D. N., Bean, R., Dore, O., et al. 2007, ApJS, 170, 377
Srivastav, S., Anupama, G. C., Sahu, D. K., & Ravikumar, C. D. 2017, MNRAS, 466, 2436
Stritzinger, M. D., Hamuy, M., Suntzeff, N. B., et al. 2002, AJ, 124, 2100
Stritzinger, M. D., Shappee, B. J., Piro, A. L., et al. 2018, ApJL, 864, L35
Strolger, L.-G., Smith, R. C., Suntzeff, N. B., et al. 2002, AJ, 124, 2905
Sullivan, M., Le Borgne, D., Prichet, C. J., et al. 2006, ApJ, 648, 868
Taubenberger, S. 2017, in Handbook of Supernovae, ed. A. Alsabti & P. Murdin (Cham: Springer), 317
Taubenberger, S., Hachinger, S., Pignata, G., et al. 2008, MNRAS, 385, 75
Tolstoy, E., Hill, V., & Tosi, M. 2009, ARA&A, 47, 371
Townsley, D. M., Miles, B. J., Shen, K. J., & Kasen, D. 2019, ApJL, 878, L38
Trujillo, I., Aguerri, J. A. L., Cepa, J., & Gutierrez, C. M. 2001, MNRAS, 328, 977
Valenti, S., Benetti, S., Cappellaro, E., et al. 2008, MNRAS, 383, 1485
Valentinuzzi, T., Poggianti, B. M., Fasano, G., et al. 2011, A&A, 536, 34
Webbink, R. F. 1984, ApJ, 277, 355
Whelan, J., & Iben, I., Jr. 1973, ApJ, 186, 1007
Wu, H., Yan, H.-J., & Zou, Z.-L. 1995, A&A, 294, L9
Wygoda, N., Elbaz, Y., & Katz, B. 2019, MNRAS, 484, 3951
Yamanaka, M., Maeda, K., Kawabata, M., et al. 2014, ApJL, 782, L35
Yuan, F., Kobayashi, C., Schmidt, B. P., et al. 2013, MNRAS, 432, 1680